

## RESEARCH ARTICLE

10.1002/2016TC004242

## Key Points:

- The MCT and ST exhibit inverted thermal field gradients, which are separated by sections of constant temperature
- The steep MCT gradient formed from ~100 to 250 km of translation on a 1 km thick shear zone, delineated by the limits of inverted metamorphism
- Translation on the MCT was accompanied by tens of km of transport-parallel stretching of hanging wall and footwall rocks

## Supporting Information:

- Supporting Information S1

## Correspondence to:

S. P. Long,  
sean.p.long@wsu.edu

## Citation:

Long, S. P., S. M. Gordon, J. P. Young, and E. Soignard (2016), Temperature and strain gradients through Lesser Himalayan rocks and across the Main Central thrust, south central Bhutan: Implications for transport-parallel stretching and inverted metamorphism, *Tectonics*, 35, 1863–1891, doi:10.1002/2016TC004242.

Received 17 MAY 2016

Accepted 18 JUL 2016

Accepted article online 22 JUL 2016

Published online 16 AUG 2016

# Temperature and strain gradients through Lesser Himalayan rocks and across the Main Central thrust, south central Bhutan: Implications for transport-parallel stretching and inverted metamorphism

Sean P. Long<sup>1</sup>, Stacia M. Gordon<sup>2</sup>, John P. Young<sup>3</sup>, and Emmanuel Soignard<sup>4</sup>
<sup>1</sup>School of the Environment, Washington State University, Pullman, Washington, U.S.A., <sup>2</sup>Department of Geological Sciences and Engineering, University of Nevada, Reno, Nevada, U.S.A., <sup>3</sup>School of Mechanical and Materials Engineering, Washington State University, Pullman, Washington, U.S.A., <sup>4</sup>LeRoy Eyring Center for Solid State Science, Arizona State University, Tempe, Arizona, U.S.A.

**Abstract** In order to understand mass and heat transfer processes that operated during Himalayan orogenesis, we collected temperature, finite and incremental strain, and kinematic vorticity data through a 5 km thickness of Lesser and Greater Himalayan rocks in southern Bhutan. This transect crosses two major shear zones, the Main Central thrust (MCT) and Shumar thrust (ST). Raman spectroscopy on carbonaceous material and garnet-biotite thermometry are integrated with deformation temperatures from quartz petrofabrics. These data define inverted field gradients that correspond in structural position with the MCT and ST, which are separated by sections in which temperatures remain essentially constant. Temperatures increase from ~400–500°C to ~700–750°C between 675 m below and 200 m above the MCT. This defines a  $269 \pm 44^\circ\text{C}/\text{km}$  inverted gradient, interpreted to have formed via high-magnitude (~100–250 km) shearing on a discrete MCT zone delineated by the limits of inverted metamorphism. Temperatures increase from ~300–400°C to ~400–530°C across the ST, which is attributed to differences in maximum burial depth of hanging wall and footwall rocks. Strain and vorticity data indicate that Lesser and Greater Himalayan rocks were deformed by layer-normal flattening. Transport-parallel lengthening and foliation-normal shortening increase from 38–71% to 36–49%, respectively, between 2.3 and 1.0 km below the MCT. The MCT acted as a “stretching fault,” with translation on the order of hundreds of kilometers accompanied by transport-parallel stretching of footwall and hanging wall rocks on the order of tens of kilometers. This demonstrates that stretching accommodated between major shear zones can make a significant contribution to cumulative mass transfer.

## 1. Introduction

Accurate assessment of the mechanisms that drive mass transfer during orogenesis, and their effects on the structural and thermal architecture of a mountain belt, is critical for understanding how orogenic systems evolve [e.g., Dahlstrom, 1969; Ramsay, 1969; Sanderson, 1982; Davis et al., 1983; Tikoff and Fossen, 1993; Mitra, 1994; Beaumont et al., 2001; Kohn, 2008]. However, in orogenic belts that exhume ductilely deformed rocks, evaluation of kinematic paths can be challenging, as diffuse strain can be complexly partitioned between structures of various scales and styles, ranging from regional shear zones to grain-scale fabrics [e.g., Sanderson, 1982; Means, 1994]. The Himalayan orogenic belt (Figure 1a), which accommodates continental convergence between India and Asia, exposes a series of deeply exhumed shear zones that bound packages of internally deformed metamorphic rocks [e.g., Gansser, 1964; LeFort, 1975; Yin and Harrison, 2000]. The Himalayan orogen therefore represents an ideal locality to investigate mass and heat transfer processes that operate at midcrustal levels during orogenesis.

The Main Central thrust (MCT), a shear zone mapped along the length of the orogen, played a major role in the southward emplacement and exhumation of high-grade Greater Himalayan (GH) rocks in its hanging wall [e.g., Gansser, 1964; LeFort, 1975; Grujic et al., 1996; Robinson et al., 2003; Yin and Harrison, 2000; Yin, 2006] and features prominently in all models of Himalayan evolution [e.g., Grujic et al., 1996; Beaumont et al., 2001, 2004; Robinson et al., 2003; Jamieson et al., 2004; Godin et al., 2006; Webb et al., 2007; Kohn, 2008; Corrie et al., 2012]. The MCT is delineated by an inverted metamorphic field gradient, expressed by telescoped mineral isograds and a corresponding structurally upward increase in apparent deformation and peak temperatures [e.g.,

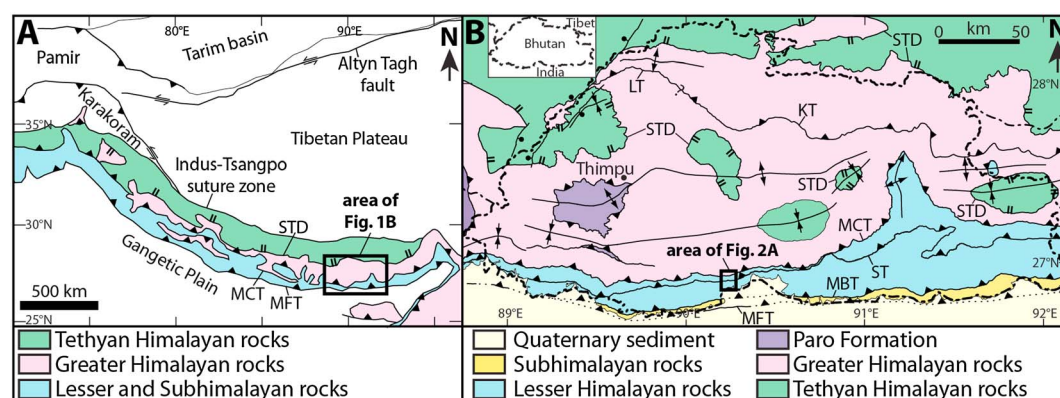


**Figure 1.** (a) Generalized geologic map of the Himalayan-Tibetan orogen, showing tectonostratigraphic divisions of the Himalayan thrust belt (simplified from Yin [2006]). (b) Simplified geologic map of Bhutan (modified from Long *et al.* [2012]). Inset box shows the location of Figure 2a. Structure abbreviations: MFT, Main Frontal thrust; MBT, Main Boundary thrust; ST, Shumar thrust; MCT, Main Central thrust; STD, South Tibetan detachment system; KT, Kakhtang thrust; LT, Laya thrust.

Gansser, 1964, 1983; LeFort, 1975; Harrison *et al.*, 1997, 1998; Hodges, 2000; Catlos *et al.*, 2001; Yakymchuk and Godin, 2012; Law *et al.*, 2013; Mottram *et al.*, 2014; Kohn, 2014]. However, the origin and tectonic significance of inverted metamorphism across the MCT is actively debated. Several mechanisms have been proposed, including downward heat conduction from emplacement of hot GH rocks [LeFort, 1975], postmetamorphic distributed shearing of upright isotherms [e.g., Grujic *et al.*, 1996; Vannay and Grasemann, 2001], and long-distance structural transport through a thermal regime of folded isotherms [e.g., Kohn, 2008, 2014].

Within the Himalayan thrust belt, and in ductile thrust belts in general, it is often difficult to decipher the relative significance of displacement within map-scale shear zones versus internal strain accommodated within rocks between shear zones. To complicate this, many Himalayan studies debate the thickness of first-order shear zones. For example, interpretations of the MCT range from a discrete zone of intense penetrative shear as thin as 0.5 km to a >10 km thick, diffuse zone of distributed shear [e.g., Grujic *et al.*, 1996, 2002; Vannay and Grasemann, 2001; Searle *et al.*, 2008; Law *et al.*, 2013]. Studies that quantify the vorticity of shearing in transects across the MCT [e.g., Grasemann *et al.*, 1999; Jessup *et al.*, 2006; Law *et al.*, 2013] have made significant advances in understanding general strain paths in this shear zone. However, prevalent dynamic recrystallization in these intensely sheared rocks inhibits delineating the upper and lower limits of the MCT on the basis of finite strain magnitude [e.g., Grasemann *et al.*, 1999; Long *et al.*, 2011c].

Here we integrate metamorphic and deformation temperatures, 3-D finite and incremental analyses of quartz crystal-plastic strain, and estimates of mean kinematic vorticity to quantify field gradients through a 5 km thick section of Lesser Himalayan (LH) and GH rocks in the Himalayan thrust belt in south central Bhutan (Figure 1b). This transect crosses two first-order shear zones, the Shumar thrust (ST), an intra-LH structure that is correlated across the width of Bhutan [Long *et al.*, 2011b, 2011d] and the more extensively studied MCT. The field gradients obtained from our data are then used to address several Himalayan questions, including differentiating among hypotheses for the origin of inverted metamorphism, and the relative contributions of offset on major shear zones versus internal strain accommodated within rocks between them.

## 2. Himalayan Tectonic Framework

The Himalayan-Tibetan orogenic system is the product of Cenozoic collision and continued convergence between the Indian and Asian plates [e.g., Gansser, 1964; LeFort, 1975; Hodges, 2000; Yin, 2006]. At the southern end of the orogen, the south vergent Himalayan thrust belt has deformed a composite series of sedimentary basins deposited on the northern margin of Greater India [e.g., Powell and Conaghan, 1973; LeFort, 1975; Mattauer, 1986; DeCelles *et al.*, 2002; Yin, 2006]. First-order thrust faults and shear zones, many of which can be correlated along the length of the orogen, have been used to separate the thrust belt into tectonostratigraphic divisions (Figure 1a) [e.g., Gansser, 1964; Yin, 2006]. In the south, the Main Frontal thrust places Neogene synorogenic sedimentary rocks, referred to as Subhimalayan rocks, over modern foreland basin

sediments. Farther north, the LH section is composed of Precambrian to Paleozoic sedimentary rocks that were variably buried and metamorphosed, typically to greenschist facies conditions, during Himalayan orogenesis. LH rocks overlie Subhimalayan rocks across the Main Boundary thrust and are deformed into a south vergent thrust belt characterized by regional duplex systems [e.g., Robinson *et al.*, 2006; Long *et al.*, 2011b; Webb, 2013]. To the north, the GH section consists of dominantly upper amphibolite facies metasedimentary and metaigneous rocks, which are locally migmatitic. GH rocks were buried to midcrustal levels early during Himalayan orogenesis and were subsequently emplaced over LH rocks across the top-to-south MCT [e.g., Gansser, 1964; LeFort, 1975].

The kingdom of Bhutan lies in the eastern part of the orogen (Figure 1b). Bhutan exhibits the characteristic Himalayan architecture of GH rocks overlying LH rocks across the MCT and LH rocks overlying Subhimalayan rocks across the Main Boundary thrust [Gansser, 1983; Bhargava, 1995; Long *et al.*, 2011d]. However, the ST is an additional first-order structure mapped within the LH section along the length of Bhutan [McQuarrie *et al.*, 2008; Long *et al.*, 2011d]. In eastern Bhutan, the ST acted as the roof thrust for a structurally lower LH duplex and as the floor thrust for a structurally higher LH duplex [Long *et al.*, 2011b, 2012].

### 3. Tectonostratigraphy of the Sarpang Transect

Geologic mapping was performed along a road northwest of the town of Sarpang in south central Bhutan (Figure 2a). Fifty-six separate outcrops were examined, with samples collected from 39 of these localities. Rocks at all localities exhibited a macroscopic foliation, which consistently dips northward (Figure 2a inset). Mineral-stretching lineations were observed in most outcrops, and trend approximately northward (Figure 2a inset). Structural thicknesses (thickness measured normal to foliation; all thicknesses listed below are structural thicknesses and are rounded to the nearest 25 m) were measured by projecting structures, contacts, and the apparent dip of foliation measurements onto a cross section (Figure 2b). The field stops and sample localities are shown in a tectonostratigraphic column (Figure 3) with structural distance relative to the MCT. The transect encompasses a total thickness of 5100 m, ranging from 4400 m below to 700 m above the MCT. On average, field stops below the ST are spaced ~125 m apart, stops between the ST and the MCT are spaced ~75 m apart, and stops above the MCT are spaced ~100 m apart (Figure 3). Below, lithologies of LH and GH rocks along the Sarpang transect are described from structurally lowest to highest position, and the criteria used to map the ST and MCT are defined.

#### 3.1. Manas Formation

The LH Manas Formation is characterized by medium gray, thick-bedded, coarse-grained quartzite (Figure 4a) interlayered with dark gray phyllite [Tangri, 1995; Long *et al.*, 2011a]. In thin section, quartzite and phyllite exhibit neoblastic muscovite, which often grows in strain shadows between elongate quartz grains (Figure 5a). Several phyllite samples also contain chlorite (Figure 5b). At the southern end of the transect, the Manas Formation is covered by Quaternary sediment, which is deposited within a 40 km wide embayment into the orogenic front (Figure 1b). To the east and west of this embayment, the Manas Formation overlies the Miocene-Pliocene Siwalik Group across the Main Boundary thrust (Figure 1b) [Bhargava, 1995; Long *et al.*, 2011d]. A minimum thickness of 2100 m for the Manas Formation was observed on the transect (Figure 3). Along strike in Bhutan, Manas Formation quartzite samples yield youngest detrital zircon age peaks of circa 0.9–1.0 Ga and circa 500–525 Ma, indicating a Neoproterozoic to Cambrian maximum depositional age range [Long *et al.*, 2011a; McQuarrie *et al.*, 2013].

#### 3.2. Daling Formation

The LH Daling Formation overlies the Manas Formation across the ST and consists of tan to light gray, thin-bedded, fine-grained quartzite interlayered with green phyllite and schist (Figures 4b and 4c) [Dasgupta, 1995a; Long *et al.*, 2011a]. In thin section, phyllite, schist, and quartzite exhibit neoblastic muscovite and biotite (Figure 5c). The Daling Formation is the upper unit of the Daling-Shumar Group, which is exposed along the length of Bhutan [Bhargava, 1995; Long *et al.*, 2011d]. In most places, the Daling-Shumar Group exhibits a cliff-forming quartzite unit called the Shumar Formation at its base [Long *et al.*, 2011a]. However, the Sarpang transect falls within a 130 km wide region of south central Bhutan in which the hanging wall level of the ST has cut upsection into the Daling Formation. Therefore, the Shumar Formation is not exposed [Long *et al.*, 2011d]. A minimum thickness of 1550 m for the Daling Formation is observed on the transect (Figure 3).

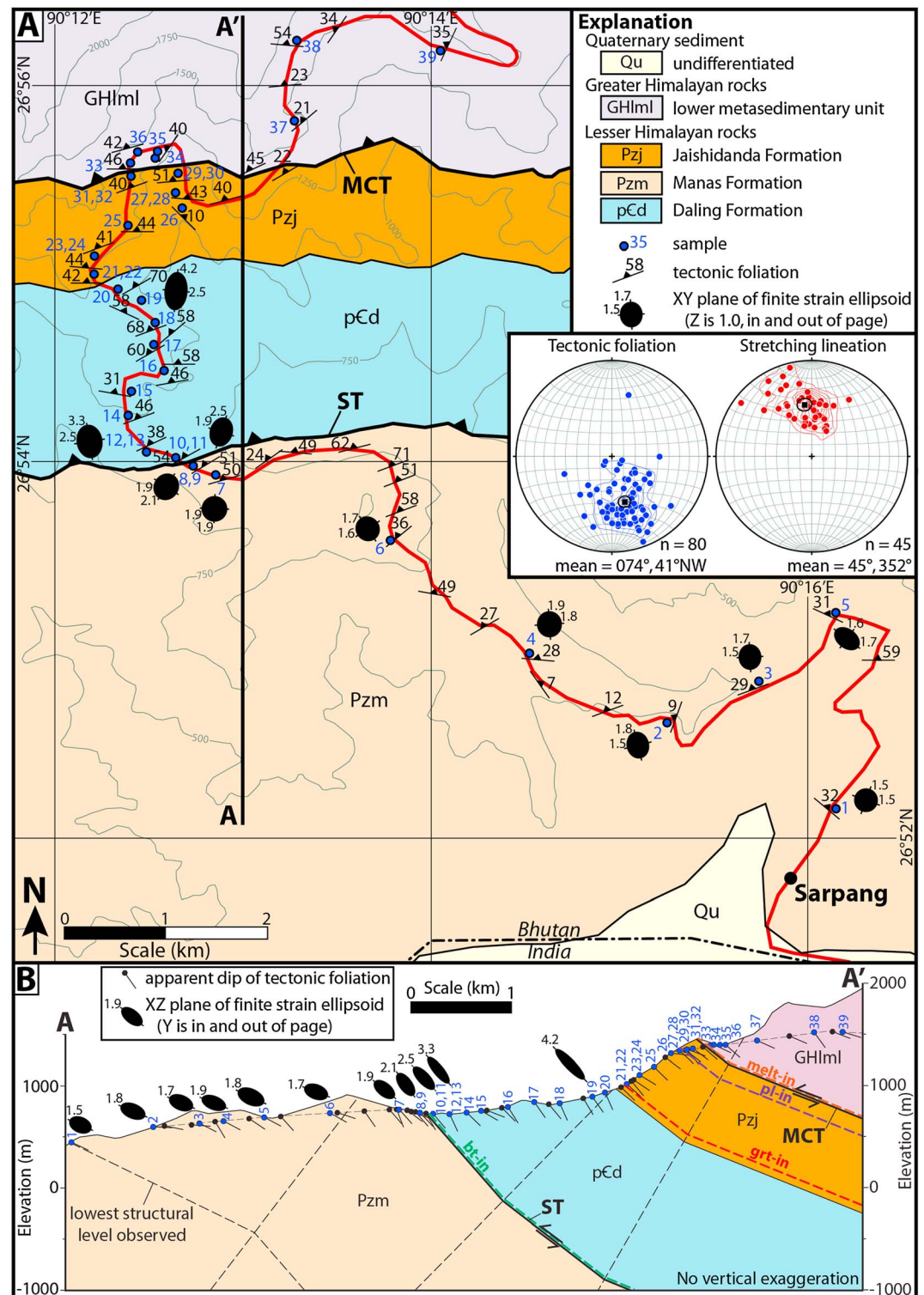


**Figure 2.** (a) Geologic map of the Sarpang transect showing structural measurements, locations of analyzed samples, and finite strain ellipsoids. Inset shows equal-area, lower hemisphere stereoplots of all measurements of tectonic foliation (poles to planes plotted) and mineral-stretching lineation (generated using Stereonet 8) [Allmendinger et al., 2011]. Mean vector and 1 $\sigma$  confidence envelope for each stereoplot is shown with black box and circle. (b) Cross section of Sarpang transect. Mineral abbreviations after Whitney and Evans [2010]. Cross section is drafted after Suppe [1983], with kink axes bisecting adjacent zones of approximately homogeneous apparent dip. For both Figures 2a and 2b, finite strain ellipsoids are scaled to constant volume. ST, Shumar thrust; MCT, Main Central thrust.



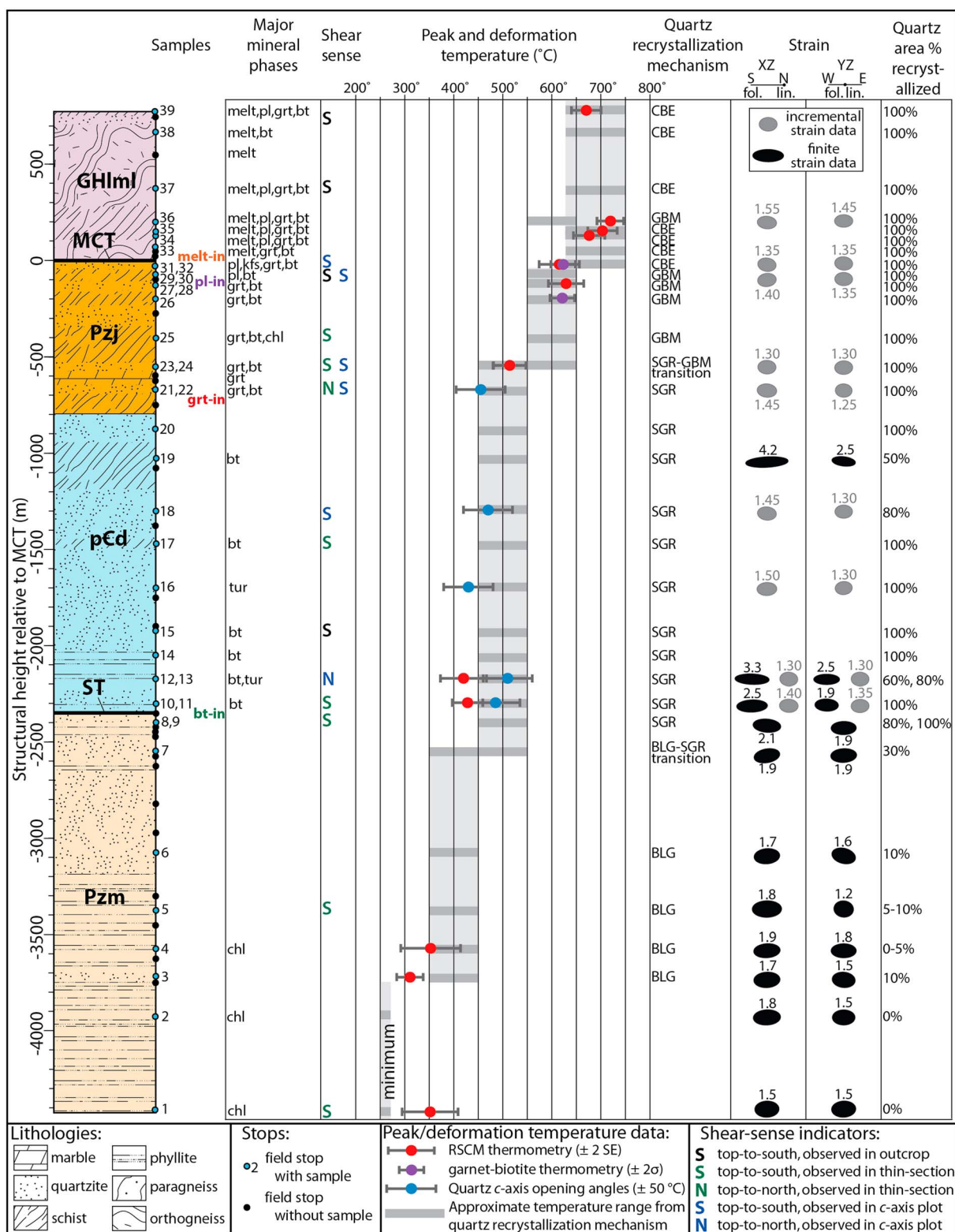


**Figure 3.** Tectonostratigraphic column of the Sarpang transect, showing major mineral phases (all samples also contain quartz and muscovite), shear sense, peak and deformation temperature, and finite and incremental strain data versus structural height (foliation-normal distance; measured from Figure 2b) relative to the MCT. Mineral abbreviations after *Whitney and Evans* [2010]. ST, Shumar thrust; MCT, Main Central thrust; BLG, bulging; SGR, subgrain rotation; GBM, grain boundary migration without chessboard extinction; CBE, grain boundary migration with chessboard extinction. See Figure 2 for explanation of rock unit abbreviations.

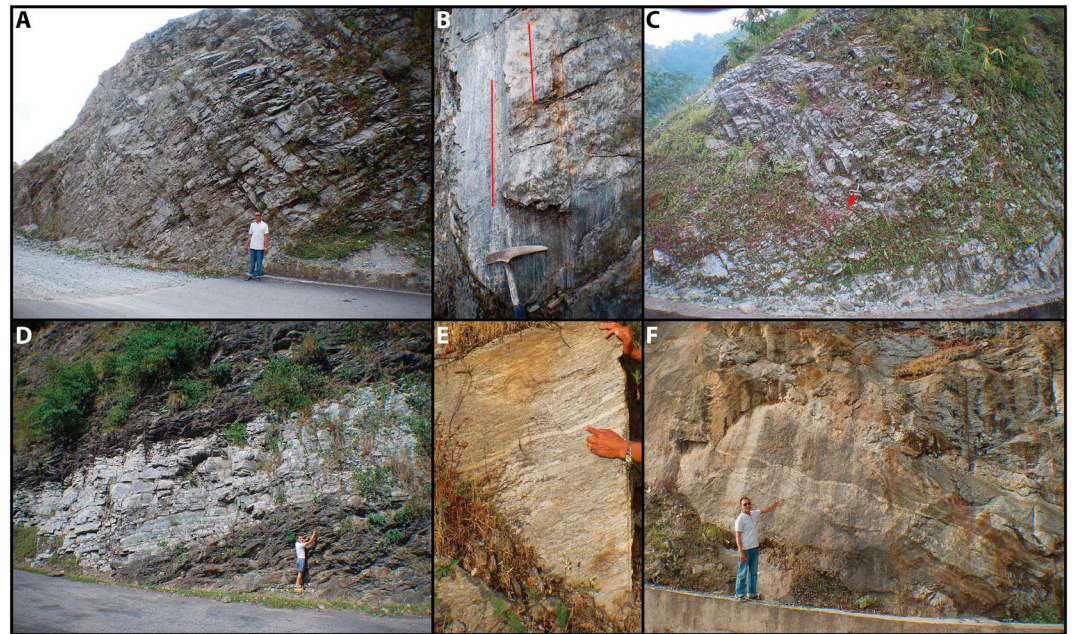


**Figure 4.** Photographs illustrating outcrop-scale lithologic characteristics of LH and GH rocks on the Sarpang transect. (a) Medium gray, thick-bedded quartzite characteristic of the Manas Formation. (b) Strongly lineated Daling Formation quartzite; view is facing down on the top of a foliation plane. Upper right part of the photo (undulose, locally rust-colored surface) is a phyllitic parting, and bottom and left parts of the photo (smooth, gray-green surface) is a quartzite foliation surface. Red lines trace mineral-stretching lineation. (c) Light gray, thin-bedded quartzite characteristic of the Daling Formation. Red arrow points to rock hammer for scale. (d) Outcrop-scale interlayering of quartzite (light gray) and biotite-rich, garnet-bearing schist (dark gray) characteristic of the Jaishidanda Formation. (e and f) Migmatitic GH orthogneiss with granitic leucosomes, which are observed in all GH outcrops examined on the Sarpang transect.

Along strike in Bhutan, Daling-Shumar Group quartzite consistently yields circa 1.8–1.9 Ga youngest detrital zircon age peaks, and in several places, the section is intruded by circa 1.75–1.85 Ga granitic plutons, indicating a Paleoproterozoic deposition age [Daniel *et al.*, 2003; Richards *et al.*, 2006; Long *et al.*, 2011a].

### 3.3. Shumar Thrust

The ST is mapped at an upsection change in quartzite lithology, from the medium gray, thick-bedded, coarse-grained quartzite of the Manas Formation, to the tan to light gray, thin-bedded, fine-grained quartzite of the Daling Formation. Daling Formation quartzite in the immediate hanging wall of the ST exhibits the structurally lowest occurrence of biotite, which indicates that the ST coincides with the biotite-in isograd (Figures 2b, 3, and 5c). In eastern Bhutan, motion on the ST is bracketed between circa 17 Ma, the timing of prograde metamorphism of rocks in its footwall at its northernmost exposed extent, and circa 10 Ma, the timing of the earliest exhumation recorded in structurally lower LH thrust sheets [Long *et al.*, 2012]. In western Bhutan, rocks in the ST hanging wall cooled rapidly from 500 to 180°C between circa 15 and 9 Ma, which is interpreted as the approximate duration of motion on the ST [McQuarrie *et al.*, 2014].

### 3.4. Jaishidanda Formation

The LH Jaishidanda Formation overlies the Daling Formation, and this contact has been interpreted as an unconformity that was subsequently sheared during Himalayan orogenesis [McQuarrie *et al.*, 2008; Long *et al.*, 2011a]. The Jaishidanda Formation consists of dark gray, biotite-rich, locally garnet-bearing schist, interlayered with medium to dark gray, thin- to medium-bedded quartzite [Long *et al.*, 2011a]. The quartzite commonly exhibits biotite-rich compositional laminations or biotite schist partings [Dasgupta, 1995b; McQuarrie *et al.*, 2008; Long *et al.*, 2011a]. Outcrop-scale interlayering of quartzite and schist is characteristic of the Jaishidanda Formation (Figure 4d). The basal contact is distinguished by the upsection transition from pure quartzite of the Daling Formation, which contains sparse biotite and muscovite, to the biotite-rich quartzite of the Jaishidanda Formation. This difference in the volume proportion of biotite is interpreted to



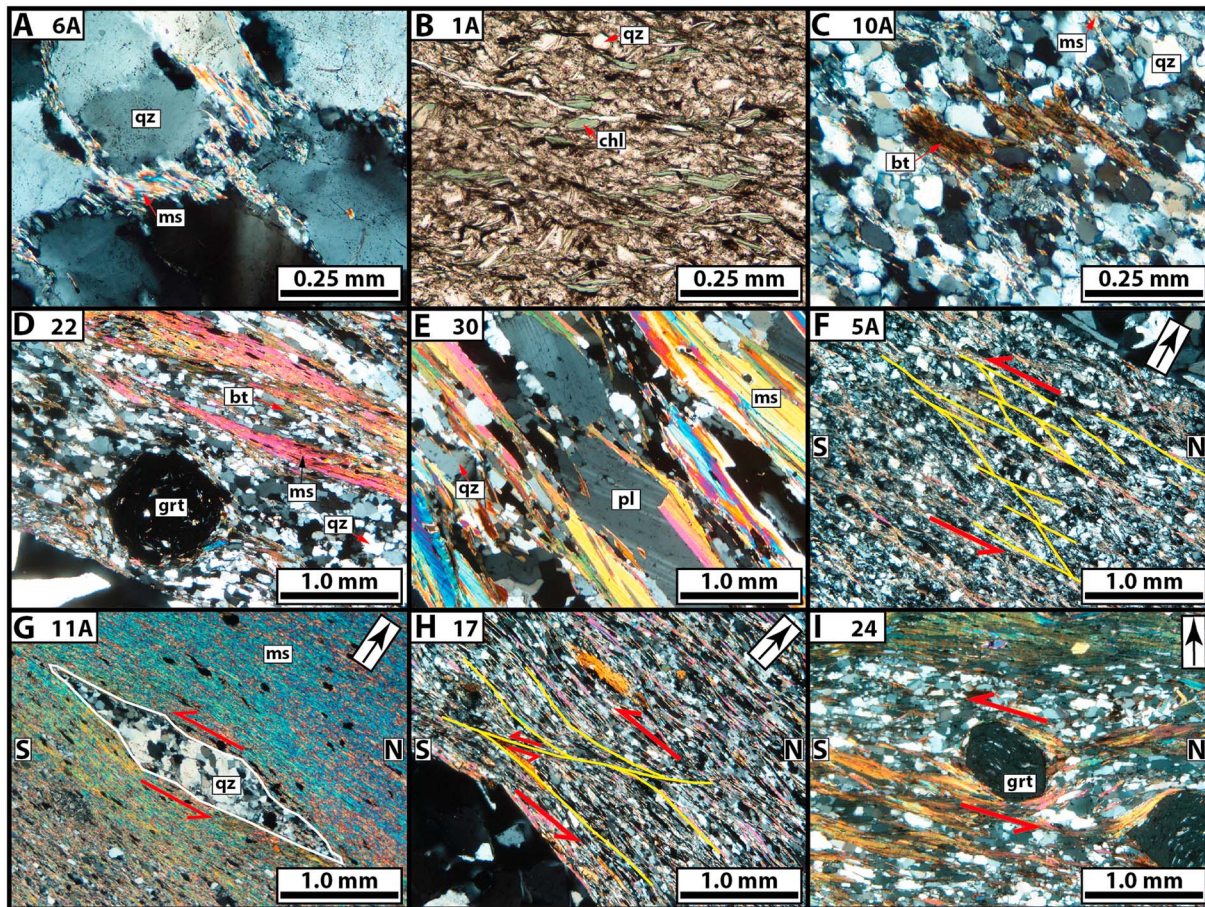


**Figure 5.** Photomicrographs illustrating mineral assemblages observed on the Sarpang transect: (a) Neoblastic muscovite, growing within strain shadows between elongate quartz porphyroclasts in Manas Formation quartzite. (b) Chlorite within Manas Formation phyllite. (c) Structurally lowest biotite porphyroblast observed on transect, within Daling Formation quartzite 50 m above ST. (d) Structurally lowest garnet porphyroblast observed on transect, within muscovite-biotite-garnet schist in lower part of Jaishidanda Formation. (e) Structurally lowest plagioclase porphyroblast observed on transect, within muscovite-biotite-garnet-plagioclase schist in upper part of Jaishidanda Formation, 75 m below MCT. Photomicrographs illustrating representative shear sense indicators observed on the Sarpang transect ("N" and "S" show north and south, respectively, the black arrow points structurally upward, and the red arrows show the sense of shear): (f) Top-to-south SC fabric within Manas Formation phyllite 1025 m below ST. (g) Top-to-south quartz  $\sigma$  object within Daling Formation phyllite 50 m above ST. (h) Top-to-south C'-type shear band within Daling Formation schist 875 m above ST. (i) Top-to-south elongate and rotated garnet porphyroblast within Jaishidanda Formation schist 550 m below MCT. Mineral abbreviations after *Whitney and Evans* [2010]. All photomicrographs taken on foliation-normal, lineation-parallel thin sections. Photo in Figure 5b was taken in plane-polarized light; all other photos taken in cross-polarized light.

reflect a difference in protolith [Long *et al.*, 2011a]. In multiple transects across Bhutan, this protolith change also corresponds to a marked change in detrital zircon age spectra. Jaishidanda Formation quartzite yields youngest detrital zircon age peaks of circa 1.0–0.8 Ga and circa 550–475 Ma [McQuarrie *et al.*, 2013; Long *et al.*, 2011a], indicating a Neoproterozoic to Ordovician maximum depositional age range. Moving structurally higher in the Jaishidanda Formation, garnet porphyroblasts (Figure 5d; sample 22) and plagioclase (Figure 5e; sample 30) are first observed in schist 125 m and 725 m above the basal contact, respectively (Figures 2a and 3). The highest outcrop mapped as the Jaishidanda Formation is 775 m above the basal contact (samples 31 and 32).

### 3.5. Greater Himalayan Rocks

Approximately 825 m above the basal Jaishidanda Formation contact, migmatitic granitic orthogneiss is observed (Figures 4e and 4f), marking a distinct change in protolith and metamorphic grade. This protolith change is interpreted to delineate the MCT and the upsection transition to rocks of GH affinity [e.g., Gansser, 1983; Bhargava, 1995; Grujic *et al.*, 2002; Daniel *et al.*, 2003; Long *et al.*, 2011b]. The basal GH orthogneiss is ~125 m thick and is overlain by ~250 m of migmatitic, garnet-bearing paragneiss, and schist

(samples 34–36). Between ~375 and 750 m above the MCT, migmatitic orthogneiss is again observed (samples 37 and 38). The highest examined outcrop (775 m above the MCT) consists of migmatitic, garnet-bearing schist interlayered with quartzite (sample 39). Kyanite and sillimanite were not observed in any of the metasedimentary GH rocks on the Sarpang transect.

Following the mapping of Long *et al.* [2011d], these rocks are assigned to the GH lower metasedimentary unit. Across Bhutan, quartzite from the lower metasedimentary unit yields youngest detrital zircon age peaks between circa 0.7 and 1.0 Ga [Long and McQuarrie, 2010; McQuarrie *et al.*, 2013], indicating a Neoproterozoic maximum depositional age for sedimentary protoliths. Quartzite from locality 37 yielded a circa 970 Ma youngest detrital zircon age peak (sample BU10-20 from McQuarrie *et al.* [2013]). Orthogneiss bodies observed within GH rocks across the Himalayan orogen have been interpreted as granitic plutons that intruded GH sedimentary protoliths and were subsequently deformed during Himalayan orogenesis [e.g., Gehrels *et al.*, 2003; Cawood *et al.*, 2007]. In eastern Bhutan, a circa 480–500 Ma U-Pb zircon crystallization age obtained from orthogneiss just above the MCT provides a Cambrian–Ordovician upper bound on the depositional age of sedimentary protoliths of the GH lower metasedimentary unit [Long and McQuarrie, 2010].

### 3.6. Main Central Thrust

There has been general agreement on the mapped location of the MCT in previous studies in Bhutan [e.g., Gansser, 1983; Bhargava, 1995; Grujic *et al.*, 1996, 2002; Davidson *et al.*, 1997; Daniel *et al.*, 2003; Long and McQuarrie, 2010; Long *et al.*, 2011b, 2011d; Corrie *et al.*, 2012]. Earlier studies mapped the MCT at the base of the lowest observed gneiss [Gansser, 1983; Bhargava, 1995]. More recent studies have documented that the first appearances of gneissic banding and granitic leucosomes usually occur within an interval of rock that is only a few tens of meters structural thickness [Daniel *et al.*, 2003; Long *et al.*, 2011b]. In addition, where metasedimentary rocks lie within the immediate MCT hanging wall, the kyanite-in or sillimanite-in isograd often corresponds with the first appearance of gneissic banding and leucosomes [Daniel *et al.*, 2003; Long and McQuarrie, 2010; Long *et al.*, 2011b].

On the Sarpang transect, we map the MCT at the base of the lowest orthogneiss, and we document that this outcrop and all rocks examined above it are migmatitic. Aluminosilicates were not observed in any of the metasedimentary rocks above the MCT studied on this transect; however, the kyanite-in isograd corresponds with the mapped position of the MCT along the Puna Tsang Chu, 15 km to the west [Long *et al.*, 2011d].

In eastern Bhutan, initial motion on the MCT must be younger than circa 23 Ma, the timing of youngest prograde metamorphic growth of monazite in its hanging wall [Chambers *et al.*, 2011]. MCT motion continued until at least circa 16 Ma, the timing of crystallization of a sheared leucogranite body in the MCT zone [Daniel *et al.*, 2003]. In addition, prograde metamorphism of MCT footwall rocks in eastern Bhutan spans circa 21–17 Ma [Daniel *et al.*, 2003; Zeiger *et al.*, 2015]. In western Bhutan, motion on the MCT is bracketed between circa 21 Ma and circa 15 Ma, using the same geochronometric criteria [Tobgay *et al.*, 2012].

## 4. Temperature Data

Multiple temperature data sets were collected from LH and GH samples on the Sarpang transect. These data record both the conditions of deformation (deformation thermometry from quartz recrystallization microstructures and quartz petrofabrics) and peak or near-peak metamorphism (Raman spectroscopy on carbonaceous material and garnet-biotite thermometry).

### 4.1. Deformation Thermometry From Quartz Recrystallization Microstructures

The microstructures of dynamically recrystallized quartz were analyzed in thin sections of Sarpang transect samples. These microstructures can be used to interpret a dominant recrystallization mechanism and to provide semiquantitative estimates of deformation temperature [e.g., Stipp *et al.*, 2002; Law, 2014], assuming that the rocks described here were deformed at similar strain rates to those on which the Stipp *et al.* [2002] quartz recrystallization mechanism thermometer is based ( $10^{-12}$ – $10^{-14}$  s<sup>-1</sup>). Here deformation temperature ranges for bulging, subgrain rotation, and grain boundary migration recrystallization calibrated specifically for Himalayan rocks [Law, 2014] are utilized. Below, are described from structurally lowest to highest, and corresponding deformation temperature ranges are plotted on Figure 3.



Manas Formation samples 1 and 2 exhibit plastically elongated quartz porphyroclasts with undulose extinction (Figure 6a). These microstructures indicate attainment of the  $\sim 250$ – $270^\circ\text{C}$  minimum temperatures necessary for quartz crystal-plastic deformation [Dunlap *et al.*, 1997; van Daalen *et al.*, 1999; Stipp *et al.*, 2002]. However, quartz porphyroclasts in these samples do not show evidence for recrystallization.

Manas Formation samples 3–7 contain plastically elongated quartz porphyroclasts with undulose extinction (Figure 6b). Quartz typically exhibits development of  $\leq 25\text{ }\mu\text{m}$  diameter subgrains at grain boundaries (Figures 6b and 6c), which is characteristic of bulging (BLG) recrystallization [Bailey and Hirsch, 1962; Drury *et al.*, 1985; Drury and Urai, 1990], indicating deformation temperatures of  $\sim 350$ – $450^\circ\text{C}$  [Law, 2014]. The total area percentage of quartz that is recrystallized into subgrains in samples 3–6 is between  $\sim 5$  and 10%. Sample 7, which is 200 m below the ST, exhibits a  $\sim 30\%$  recrystallized area proportion and a core-and-mantle texture [e.g., Fitzgerald and Stunitz, 1993] with elongated porphyroclasts surrounded by a matrix of recrystallized grains (Figure 6d). This texture is interpreted to mark the transition from BLG to subgrain rotation (SGR)-dominated recrystallization, which occurs at  $\sim 450^\circ\text{C}$  [Law, 2014].

Manas Formation samples 8 and 9, Daling Formation samples 10–20, and Jaishidanda Formation samples 21–23 are all dominated by equigranular, polygonal,  $\sim 25$ – $50\text{ }\mu\text{m}$  diameter quartz neoblasts (defined here as visually distinct recrystallized grains) (Figures 6e and 6f). This texture is indicative of SGR recrystallization [Poirier and Nicolas, 1975; White, 1977; Guillope and Poirier, 1979], which occurs at temperatures between  $\sim 450$  and  $550^\circ\text{C}$  [Law, 2014]. Most of these samples exhibit complete recrystallization of quartz. However, five of these samples (9, 12, 13, 18, and 19) exhibit a  $\sim 50$ – $80\%$  recrystallized area proportion, with a matrix of neoblasts surrounding elongated quartz porphyroclasts (Figure 6e).

Jaishidanda Formation sample 24, located 550 m below the MCT, exhibits nucleation of “island grains” up to  $\sim 0.5\text{ mm}$  in diameter, which are surrounded by a matrix of  $\leq 0.2\text{ mm}$  diameter neoblasts characteristic of SGR recrystallization (Figure 6g). This texture is interpreted to mark the transition between SGR- and grain boundary migration (GBM)-dominated recrystallization, which occurs at  $\sim 550^\circ\text{C}$  [Law, 2014].

Between 400 and 75 m below the MCT, Jaishidanda Formation samples 25–30 contain large (locally  $\geq 1.0\text{ mm}$  diameter), “amoeboid” quartz neoblasts, which exhibit cusped, interfingering boundaries, pinning structures, and engulfing of mica grains [e.g., Dunlap *et al.*, 1997] (Figure 6h). This microstructure is characteristic of GBM recrystallization [Guillope and Poirier, 1979; Urai *et al.*, 1986], and indicates deformation temperatures of  $\sim 550$ – $650^\circ\text{C}$  [Law, 2014].

Jaishidanda Formation samples 31 and 32 (25 m below the MCT) and nearly all GH samples above the MCT contain amoeboid quartz neoblasts that locally exhibit chessboard extinction (CBE) (Figures 6i and 6j). Chessboard extinction results from slip on basal  $\langle a \rangle$  and prism  $\langle c \rangle$  planes [Lister and Dornsiepen, 1982; Blumenfeld *et al.*, 1986; Mainprice *et al.*, 1986; Kruhl, 1996] and occurs at temperatures  $\geq \sim 630^\circ\text{C}$  [Stipp *et al.*, 2002].

#### 4.2. Deformation Thermometry From Quartz Petrofabrics

Quartz petrofabrics can yield information on kinematics, 3-D strain, and deformation temperature [e.g., Lister and Williams, 1979; Lister and Hobbs, 1980; Schmid and Casey, 1986; Kruhl, 1998; Morgan and Law, 2004; Law, 2014; Faleiros *et al.*, 2016], and have been extensively employed to characterize Himalayan deformation [e.g., Grujic *et al.*, 1996; Law *et al.*, 2004, 2011, 2013; Langille *et al.*, 2010; Larson and Cottle, 2014]. Nine samples of dynamically recrystallized quartzite, consisting of five from the Daling Formation, three from the Jaishidanda Formation, and one GH sample (Figure 7 and Table 1), were collected for quartz petrofabric analysis. The orientations of quartz  $c$  and  $a$  axes were measured on polished, lineation-parallel thin sections of these samples, using an electron backscatter diffraction (EBSD) detector attached to a field emission scanning electron microscope at Washington State University (see supporting information for details on methodology). Equal-area stereoplots containing orientations of individual  $c$  axes, contoured  $c$  and  $a$  axis pole figures, and visually best fit  $c$  axis fabric skeletons [e.g., Lister and Williams, 1979; Law, 2014] are shown for all nine samples on Figure 7.

All samples yielded  $c$  axis fabrics indicative of a quartz lattice-preferred orientation. Four of the structurally lowest five samples have type I (16A, 21A) or type II (12A, 18A) crossed-girdle patterns, indicating that basal  $\langle a \rangle$ , rhomb  $\langle a \rangle$ , and prism  $\langle a \rangle$  quartz slip systems were dominant [Lister, 1977; Schmid and Casey, 1986; Passchier and Trouw, 2005]. In comparison, the structurally highest four samples (23A, 29A, 31A, and 36A)

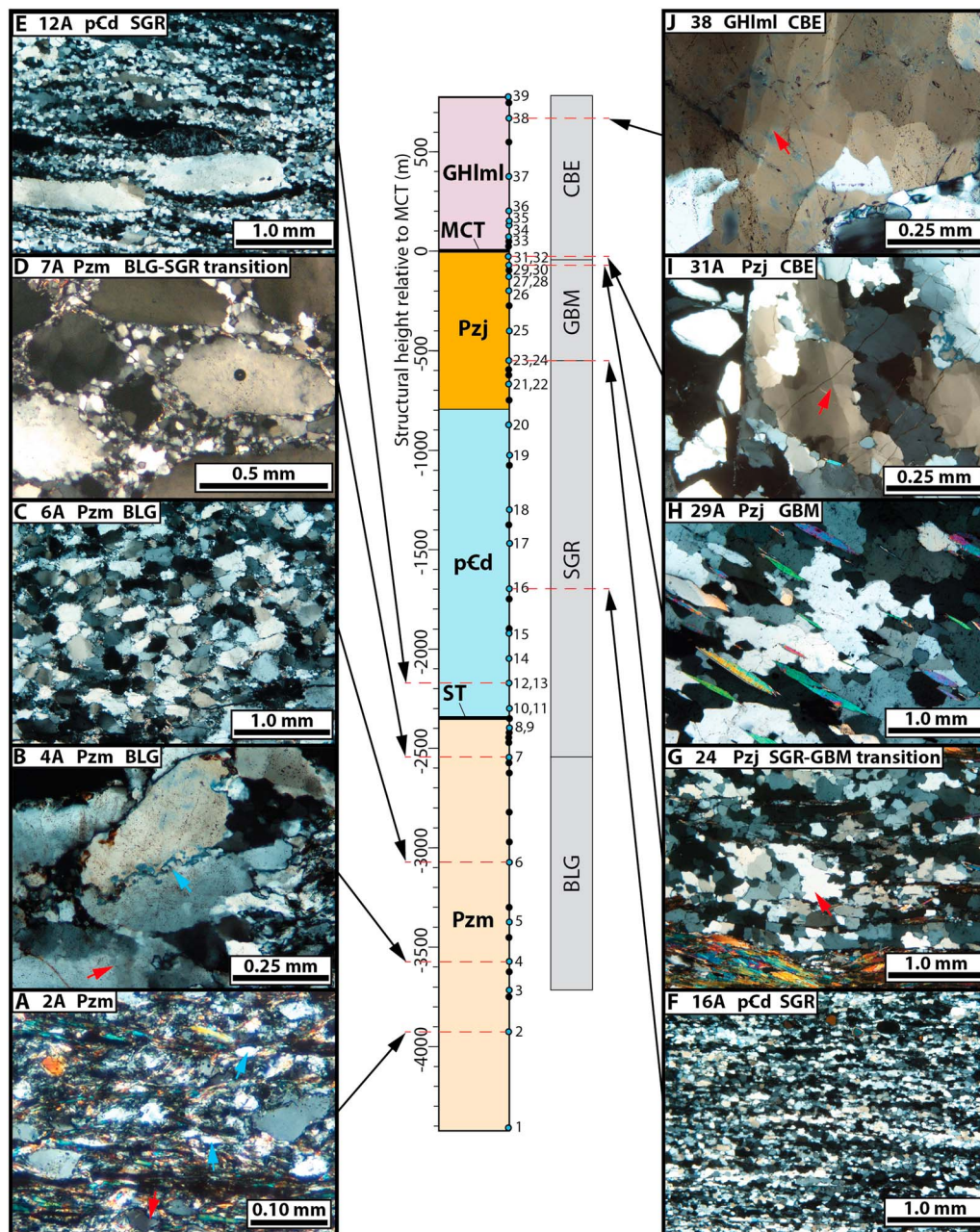


**Figure 6.** Photomicrographs (cross-polarized light) illustrating quartz recrystallization microstructures on the Sarpang transect, referenced to structural position on the tectonostratigraphic column. From structurally low to high: (a) Plastically elongated quartz porphyroclasts (blue arrows) isolated in micaceous matrix. Quartz exhibits local undulose extinction (red arrow) and no evidence for recrystallization (characteristic of Manas Formation samples 1 and 2). (b) Bulging (BLG) recrystallization localized along boundaries between adjacent quartz porphyroclasts (blue arrow) and undulose extinction (red arrow) (Manas Formation quartzite). (c) BLG microstructure characteristic of Manas Formation quartzite, with subgrains localized at quartz porphyroclast boundaries and <10% area proportion of recrystallization. (d) Transitional texture between BLG and subgrain rotation (SGR) recrystallization, consisting of core-and-mantle microstructure defined by matrix of quartz neoblasts surrounding quartz porphyroclasts, and ~30% recrystallized area proportion. This texture is only observed in Manas Formation sample 7. (e) SGR microstructure, defined by equigranular, polygonal, 25–50  $\mu\text{m}$  diameter quartz neoblasts. Neoblasts form a matrix surrounding elongated quartz ribbon porphyroclasts, defining an ~80% recrystallized area proportion; these textures are observed in some Manas Formation and Daling Formation quartzite samples. (f) SGR texture characteristic of most Daling Formation quartzite samples, in which all quartz has been recrystallized to equigranular, 25–50  $\mu\text{m}$  neoblasts. (g) Transitional texture between SGR and grain boundary migration (GBM) recrystallization, characterized by amoeboid island grains up to 0.5 mm in diameter (red arrow), surrounded by a matrix of  $\leq 0.2$  mm, equigranular quartz neoblasts. This texture is only observed in Jaishidanda Formation sample 24. (h) GBM texture, indicated by cusped, inter-fingering, amoeboid quartz grains up to 1.0 mm in diameter and engulfing of mica grains. Characteristic of Jaishidanda Formation quartzite. (i and j) GBM texture, with large (locally  $\geq 1.0$  mm diameter) quartz neoblasts exhibiting chessboard extinction (CBE), with multiple extinction domains intersecting at approximately right angles. Characteristic of most quartz-rich GH rocks. All photomicrographs were taken on thin sections that were cut normal to foliation and parallel to lineation. ST, Shumar thrust; MCT, Main Central thrust. See Figure 2 for explanation of rock unit abbreviations.



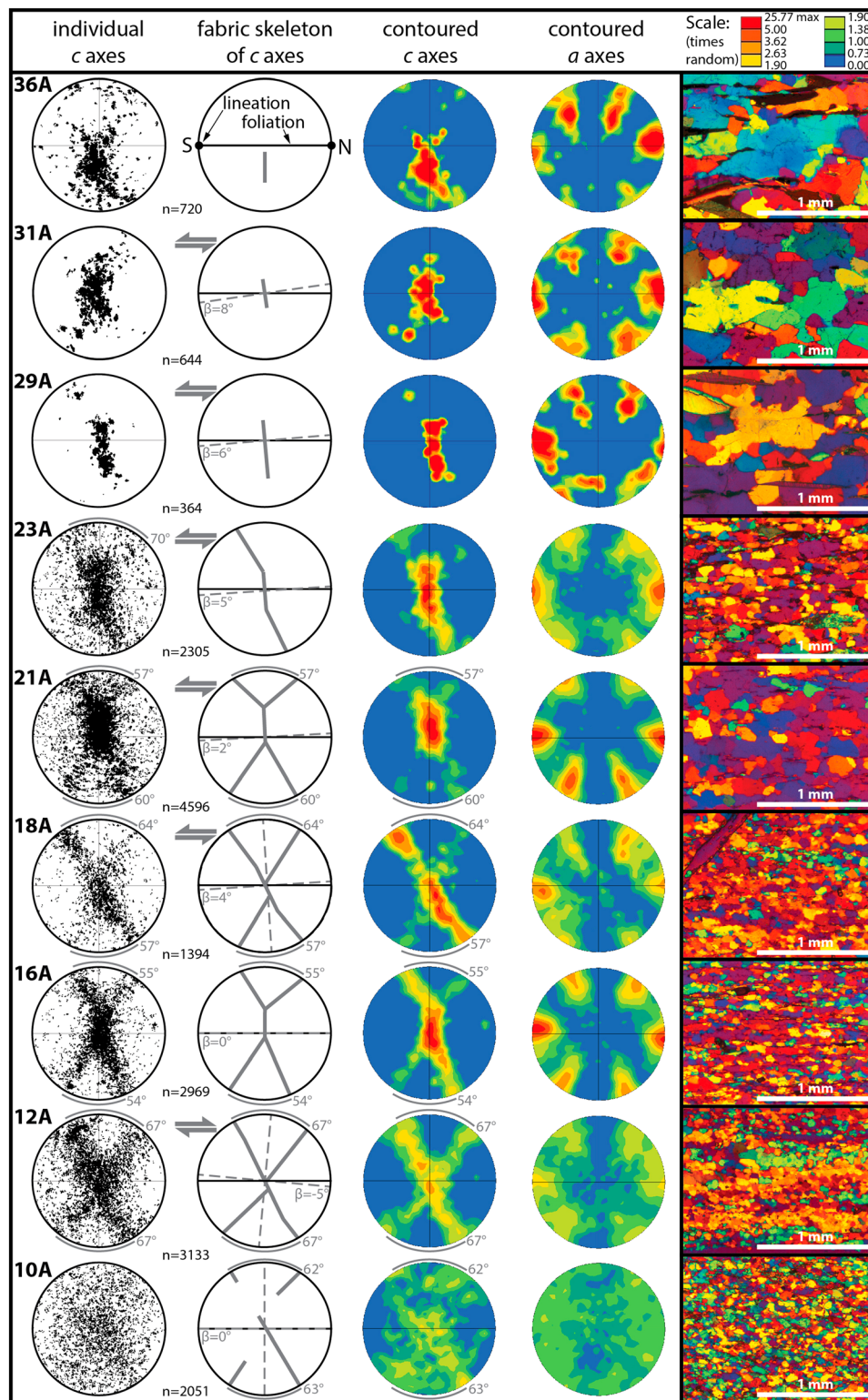


**Figure 7.** EBSD-generated quartz petrofabric data, plotted as equal-area stereographic projections. The projections are oriented with foliation as a vertical plane and lineation as a horizontal line (see example shown for sample 36A). Because stretching lineation typically trends approximately N-S, the view direction of all plots is toward the west. Vertical columns (left to right): a plot of orientations of individual *c* axes, an interpreted *c* axis fabric skeleton, a contoured *c* axis pole figure, a contoured *a* axis pole figure, and an optical photomicrograph taken with a 540 nm  $\lambda$  plate inserted are shown for each sample. Samples are ordered in ascending structural position. The number of axes measured (*n*), shear sense, fabric opening angles, and  $\beta$  angles (see supporting information) are shown. The *c* and *a* axis pole figures are all contoured relative to multiples of a random distribution and share the same scale of 5 times random.

**Table 1.** Summary of Opening Angle, Incremental Strain, and Kinematic Vorticity Data From EBSD Samples on the Sarpang Transect<sup>a</sup>

Thin Section	Map Unit	Lithology	Structural Height Relative to MCT (m)	Orientation Relative to Lineation	Average Neoblast Grain Size ( $\mu\text{m}$ , $\pm 1\sigma$ ) (n)	Quartz <i>c</i> Axis Opening Angle	Opening Angle Deformation Temperature ( $^{\circ}\text{C}$ ) <sup>b</sup>
36A	GHImI	paragneiss	200	parallel	150 $\pm$ 128 (105)	-	-
36B				perpendicular	162 $\pm$ 113 (170)		
31A	Jaishidanda	quartzite	-25	parallel	167 $\pm$ 107 (105)	-	-
31B				perpendicular	153 $\pm$ 127 (112)		
29A	Jaishidanda	quartzite	-75	parallel	176 $\pm$ 152 (91)	-	-
29B				perpendicular	176 $\pm$ 176 (116)		
23A	Jaishidanda	quartzite	-550	parallel	59 $\pm$ 35 (118)	-	-
23B				perpendicular	63 $\pm$ 32 (139)		
21A	Jaishidanda	quartzite	-675	parallel	105 $\pm$ 66 (145)	59°	455 $\pm$ 50°C
21B				perpendicular	89 $\pm$ 58 (131)		
18A	Daling	quartzite	-1300	parallel	50 $\pm$ 26 (170)	61°	470 $\pm$ 50°C
18B				perpendicular	47 $\pm$ 25 (154)		
16A	Daling	quartzite	-1700	parallel	37 $\pm$ 21 (174)	55°	430 $\pm$ 50°C
16B				perpendicular	49 $\pm$ 37 (167)		
12A	Daling	quartzite	-2175	parallel	33 $\pm$ 17 (144)	67°	510 $\pm$ 50°C
12B				perpendicular	34 $\pm$ 20 (169)		
10A	Daling	quartzite	-2300	parallel	36 $\pm$ 18 (149)	63°	485 $\pm$ 50°C
10B				perpendicular	30 $\pm$ 17 (196)		

<sup>a</sup> $\beta$  = acute angle between foliation and line normal to central axis of crossed girdle in quartz *c* axis plot [after Law *et al.*, 2013];  $\theta'_{\text{SA1}}$  = acute angle between foliation and mean angle of long axes of elongated quartz neoblasts (see supporting information);  $W_m$  = mean kinematic vorticity number for plane strain deformation;  $R_s$  = tectonic elongation (ratio of long axis to short axis);  $\phi$  = angle between long axis of strain ellipse and foliation (same as parameter  $\theta'$  of Ramsay and Huber [1983]); MCT = Main Central thrust; SPO = shape-preferred orientation; SE = standard error.

<sup>b</sup>Opening angle deformation temperatures calculated from equation (1) of Faleiros *et al.* [2016]. Temperatures are rounded to nearest 5°C and reported with  $\pm 50^{\circ}\text{C}$  error [Kruhl, 1998].

<sup>c</sup>Estimated  $W_m$  values are rounded to nearest 0.05.

<sup>d</sup>Percent pure shear values were determined from Law *et al.* [2004] and are rounded to nearest 5%.

<sup>e</sup> $R_s$  values and associated errors are rounded to nearest 0.05.

exhibit single-girdle patterns, which result from dominant slip on prism  $\langle a \rangle$  and rhomb  $\langle a \rangle$  planes [Passchier and Trouw, 2005]. The transition from crossed to single-girdle *c* axis fabrics corresponds with the structurally upward transition from SGR-dominated to GBM-dominated quartz recrystallization, which is accompanied by a significant increase in neoblast size, from  $\sim 25$ – $50 \mu\text{m}$  to  $\sim 150$ – $250 \mu\text{m}$  (Figure 7). The *c* and *a* axis fabric patterns from these samples are indicative of deformation within a 3-D strain field that approximates plane strain [e.g., Schmid and Casey, 1986].

Quartz petrofabrics can also be utilized to estimate the temperature at which the fabrics were “locked in” during the final stages of dynamic recrystallization [e.g., Law, 2014]. Kruhl [1998] presented evidence that the *c* axis opening angle of crossed-girdle fabrics is related to temperature, with increasing opening angles corresponding to higher temperatures, and updated calibrations of this thermometer have been presented in Morgan and Law [2004] and Faleiros *et al.* [2016]. Here we use the calibration of Faleiros *et al.* [2016, equation (1)] to estimate opening angle deformation temperatures. Nominal uncertainties for this thermometer are  $\pm 50^{\circ}\text{C}$  [Kruhl, 1998; Law, 2014; Faleiros *et al.*, 2016]. Opening angles can be measured for the lowest five samples (details on methodology in supporting information) (Figure 7 and Table 1). Daling Formation samples 10A, 12A, 16A, and 18A yielded average opening angles of 63°, 67°, 55°, and 61°, respectively, corresponding to temperatures of 485  $\pm$  50°C, 510  $\pm$  50°C, 430  $\pm$  50°C, and 470  $\pm$  50°C. Jaishidanda Formation sample 21A yielded an average opening angle of 59°, corresponding to a temperature of 455  $\pm$  50°C.

### 4.3. Raman Spectroscopy on Carbonaceous Material (RSCM) Thermometry

Carbonaceous material (CM), which is derived from metamorphism of organic matter, is common in metasedimentary rocks. The degree of structural organization of graphite bonds in CM is strongly temperature dependent; therefore, CM can be used to calculate metamorphic temperatures [e.g., Beyssac *et al.*, 2002, 2003; Rahl *et al.*, 2005; Aoya *et al.*, 2010]. Rahl *et al.* [2005] calibrated the RSCM thermometer for rocks that achieved temperatures between  $\sim 100$  and  $740^{\circ}\text{C}$  by measuring the height ratio (R1) and area ratio (R2) of four first-order Raman peaks (G, D1, D2, and D3) (Figure 8e) in the wave number offset range between 1200 and  $1800 \text{ cm}^{-1}$ .



**Table 1.** (continued)

$\beta$ (deg)	$\theta'_{\text{ISA1}}$ ( $\pm 1$ SE)	$W_m$ Range From Quartz SPO Method <sup>c</sup>	% Pure Shear From Quartz SPO Method <sup>d</sup>	$R_s$ ( $\pm 1$ SE) <sup>e</sup>	$\phi$ (Equal to $\theta'$ ) ( $\pm 1$ SE)	$W_m$ Range From $R_s$ Versus $\theta'$ Method <sup>c</sup>	% Pure Shear From $R_s$ versus $\theta'$ Method <sup>d</sup>
-	$5 \pm 3^\circ$	-	-	$1.55 \pm 0.10$	$5 \pm 3^\circ$	0.10–0.35	75–95%
				$1.45 \pm 0.10$	$0 \pm 2^\circ$		
$8^\circ$	$9 \pm 3^\circ$	0.45–0.65	55–70%	$1.35 \pm 0.05$	$9 \pm 3^\circ$	0.30–0.50	65–80%
				$1.35 \pm 0.05$	$6 \pm 3^\circ$		
$6^\circ$	$-7 \pm 4^\circ$	0.00–0.15	90–100%	$1.40 \pm 0.10$	$-7 \pm 4^\circ$	0.15–0.45	65–90%
				$1.35 \pm 0.10$	$1 \pm 3^\circ$		
$5^\circ$	$2 \pm 3^\circ$	0.15–0.35	75–90%	$1.30 \pm 0.10$	$2 \pm 3^\circ$	0.00–0.20	85–100%
				$1.30 \pm 0.05$	$-2 \pm 3^\circ$		
$2^\circ$	$5 \pm 3^\circ$	0.15–0.35	75–90%	$1.45 \pm 0.05$	$5 \pm 3^\circ$	0.10–0.35	75–95%
				$1.25 \pm 0.05$	$3 \pm 3^\circ$		
$4^\circ$	$6 \pm 2^\circ$	0.30–0.40	70–80%	$1.40 \pm 0.05$	$6 \pm 2^\circ$	0.20–0.35	75–85%
				$1.30 \pm 0.05$	$0 \pm 3^\circ$		
$0^\circ$	$-2 \pm 2^\circ$	0.00–0.15	90–100%	$1.50 \pm 0.10$	$-2 \pm 2^\circ$	0.00–0.20	85–100%
				$1.30 \pm 0.05$	$-5 \pm 3^\circ$		
$-5^\circ$	$4 \pm 3^\circ$	0.00–0.15	90–100%	$1.30 \pm 0.05$	$4 \pm 3^\circ$	0.05–0.30	80–95%
				$1.30 \pm 0.05$	$2 \pm 3^\circ$		
$0^\circ$	$3 \pm 3^\circ$	0.00–0.20	85–100%	$1.40 \pm 0.05$	$3 \pm 3^\circ$	0.00–0.25	80–100%
				$1.35 \pm 0.05$	$-2 \pm 3^\circ$		

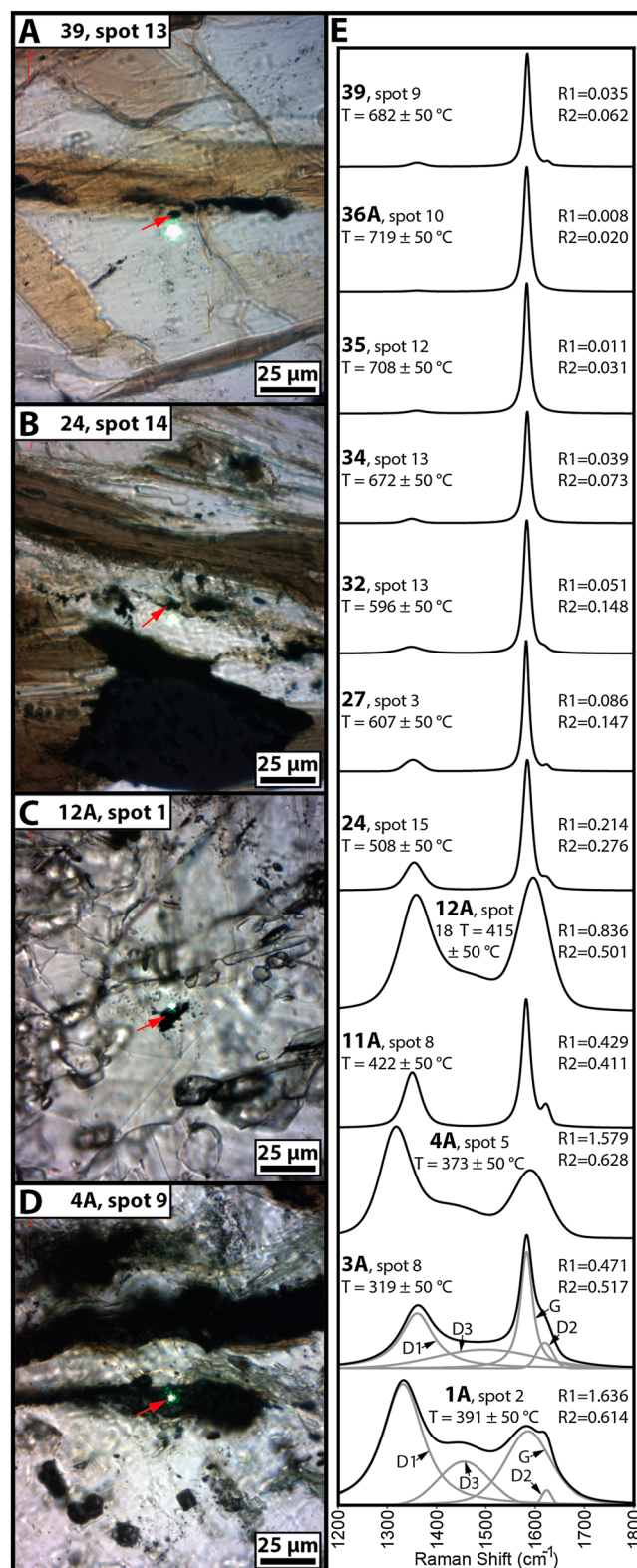
Carbonaceous material was analyzed in situ from 12 samples of LH and GH metasedimentary rocks (Table 2). Measurements were made using a Raman spectrometer at Arizona State University (see supporting information for details on methodology and data from individual analyses). The laser was focused on CM situated beneath a transparent grain (typically quartz), after procedures outlined in *Beyssac et al.* [2003]. CM was most often present as isolated  $\leq 10 \mu\text{m}$  patches (Figures 8b and 8c) and occasionally occurred within foliation-subparallel microlithons (Figures 8a and 8d). Examples of representative Raman spectra from each sample are shown in Figure 8e. Mean peak temperatures of multiple measurements, calculated using the calibration of *Rahl et al.* [2005], are shown on Table 2. After *Cooper et al.* [2013], peak temperatures are reported with 2 standard errors (SE), which takes into account internal uncertainty and the external uncertainty from the *Rahl et al.* [2005] calibration (see Table 2 footnote).

Phyllite and quartzite from the Manas Formation (samples 1A, 3A, and 4A), collected between 2100 and 1200 m below the ST, yielded RSCM temperatures of  $352 \pm 57^\circ\text{C}$ ,  $311 \pm 27^\circ\text{C}$ , and  $353 \pm 61^\circ\text{C}$ , respectively. Daling Formation phyllite sample 11A, collected 50 m above the ST, yielded a temperature of  $428 \pm 31^\circ\text{C}$ , and Daling Formation quartzite sample 12A, collected 200 m above the ST, yielded a temperature of  $420 \pm 47^\circ\text{C}$ . Schist and quartzite from the Jaishidanda Formation yielded temperatures of  $514 \pm 33^\circ\text{C}$  at 550 m below the MCT (sample 24),  $629 \pm 36^\circ\text{C}$  at 125 m below the MCT (sample 27), and  $615 \pm 41^\circ\text{C}$  (sample 32) at 25 m below the MCT. Four GH schist and paragneiss samples (34, 35, 36A, and 39), collected between 125 and 775 m above the MCT, yielded temperatures of  $676 \pm 32^\circ\text{C}$ ,  $703 \pm 30^\circ\text{C}$ ,  $719 \pm 27^\circ\text{C}$ , and  $670 \pm 30^\circ\text{C}$ , respectively.

#### 4.4. Garnet-Biotite Thermometry

Garnet and biotite from two Jaishidanda Formation schist samples (26 and 32) were also analyzed to determine peak metamorphic temperatures. The samples were collected 200 m and 25 m below the MCT, respectively. The garnet-biotite calibration 5AV of *Holdaway* [2000] was used to calculate temperatures and associated  $2\sigma$  errors, and garnet and biotite were analyzed using a JEOL 8500 F electron microprobe at Washington State University (see supporting information for details on methodology).

In sample 26, garnet porphyroblasts are typically euhedral to subhedral and are slightly elongate parallel to foliation. The garnet contain quartz, biotite, and muscovite inclusions, and the euhedral garnet have sigmoidal inclusion trails. Foliation is defined by biotite and muscovite that wrap around the garnet porphyroblasts. All garnet crystals exhibit uniform grossular ( $X_{\text{Ca}} = 0.08$ ), spessartine ( $X_{\text{Mn}} = 0.06$ ), and pyrope ( $X_{\text{Mg}} = 0.14$ ) contents, with a slight increase ( $X_{\text{Ca}} = 0.10$ ) and then decrease in grossular ( $X_{\text{Ca}} = 0.09$ ), a slight decrease ( $X_{\text{Mg}} = 0.13$ ;  $\text{Mg\#} = 0.15$ ) and then increase ( $X_{\text{Mg}} = 0.14$ ;  $\text{Mg\#} = 0.16$ ) in pyrope and  $\text{Mg\#}$ , a decrease in spessartine ( $X_{\text{Mn}} = 0.05$ ), and an increase in almandine ( $X_{\text{Fe}} = 0.72$ ) at the outermost rim (Figure 9). Almandine



and the Mg# show some variability within the core of the garnet ( $X_{\text{Fe}} = 0.72\text{--}0.73$ ;  $\text{Mg\#} = 0.16\text{--}0.17$ ). Biotite shows no zoning and little variation in Fe# (0.49–0.51) across the sample. In comparison, Ti is more variable, ranging from 0.04 to 0.10 (atoms per formula unit (apfu) normalized on the basis of 11 O atoms) for biotite included in and adjacent to garnet and  $\text{Ti} = 0.10\text{--}0.14$  for matrix grains. As the outermost rim of the garnet shows retrogression effects, the near-rim garnet and matrix biotite were used to calculate a near-peak temperature estimate of  $621 \pm 25^{\circ}\text{C}$  (see Table S3 in the supporting information).

In sample 32, the garnet porphyroblasts are typically subhedral and show some resorption/breakdown at their margins. Moreover, some porphyroblasts are elongate parallel to foliation. The porphyroblasts are inclusion-rich, with mainly quartz, graphite, and lesser biotite and muscovite found as inclusions. Biotite and muscovite define the foliation, which wraps around garnet. The garnet shows a more classic “bell-shaped” chemical zoning profile, suggesting preservation of the prograde growth history (Figure 9) [Tracy *et al.*,

**Figure 8.** (a–d) Photomicrographs (plane-polarized light) of representative examples of analyzed carbonaceous material (CM). Green spot in each photo is the Raman laser beam. In Figures (8a–8c), the beam has been moved to provide a clear view of the analyzed CM spot, which is located with a red arrow. Figures 8a and 8d illustrate foliation-subparallel microlithons of CM, and Figures 8b and 8c illustrate the more common occurrence of CM as isolated 5–10  $\mu\text{m}$  patches. (e) Examples of representative Raman spectra from single-spot analyses of each of the 12 samples. The positions of the graphite band (G) and defect bands (D1, D2, D3) are labeled on the bottom two spectra. Samples are stacked in order of increasing structural height. Peak temperatures (T) and R1 and R2 parameters are calculated after Rahl *et al.* [2005]. Peak center position, height, amplitude, and area are listed for individual spots in the supporting information. The analyses are listed with errors of  $\pm 50^{\circ}\text{C}$ , which is the external uncertainty from the Rahl *et al.* [2005] calibration.

**Table 2.** Summary of RSCM Peak Temperature Determinations From Sarpang Transect Samples<sup>a</sup>

Sample	Map Unit	Lithology	Structural Height (m)	R1		R2		Peak Temperature (°C)			n
				Mean	1 $\sigma$	Mean	1 $\sigma$	Mean	1 $\sigma$	2 SE	
39	GHlml	schist	775	0.038	0.018	0.074	0.031	670	28	30	15
36A	GHlml	paragneiss	200	0.008	0.012	0.020	0.029	719	27	27	17
35	GHlml	schist	150	0.014	0.011	0.036	0.030	703	29	30	15
34	GHlml	paragneiss	125	0.034	0.026	0.067	0.037	676	32	32	14
32	Pzj	schist	−25	0.052	0.045	0.156	0.070	615	62	41	15
27	Pzj	quartzite	−125	0.087	0.051	0.127	0.058	629	48	36	15
24	Pzj	schist	−550	0.182	0.048	0.262	0.052	514	44	33	16
12A	pCd	quartzite	−2175	0.650	0.140	0.460	0.072	420	72	47	14
11A	pCd	phyllite	−2300	0.430	0.087	0.404	0.048	428	34	31	15
4A	Pzm	phyllite	−3575	1.654	0.724	0.611	0.115	353	99	61	13
3A	Pzm	quartzite	−3725	0.553	0.149	0.541	0.034	311	16	27	15
1A	Pzm	phyllite	−4425	2.260	0.699	0.618	0.043	352	94	57	14

<sup>a</sup>R1, R2, and peak temperature values calculated using the calibration of *Rahl et al.* [2005]. Internal variability in R1, R2, and peak temperature is indicated by 1 $\sigma$  uncertainty. Temperature is also reported with 2 standard errors (SE), calculated after *Cooper et al.* [2013], from quadratic addition of 1 $\sigma$  internal error and external error of  $\pm 50^\circ\text{C}$  from the *Rahl et al.* [2005] calibration, divided by the square root of the number of analyses ( $n$ ).

1976; Yardley, 1977]. Spessartine shows a decrease from core ( $X_{\text{Mn}} = 0.11$ ) to rim ( $X_{\text{Mn}} = 0.05$ ), whereas almandine shows the opposite pattern,  $X_{\text{Fe}} = 0.64$  for the core and  $X_{\text{Fe}} = 0.69$  for the rim. The Mg# and pyrope show more gradual increases from core (Mg# = 0.13;  $X_{\text{Mg}} = 0.09$ ) to rim (Mg# = 0.15;  $X_{\text{Mg}} = 0.12$ ) (Figure 9). Grossular is near homogeneous across the garnet, ranging from 0.14 to 0.15. Biotite is also homogenous, with Fe# = 0.51–0.52 and Ti = 0.09–0.14 apfu. The garnet rim and matrix biotite compositions were used to calculate a near-peak temperature of  $623 \pm 25^\circ\text{C}$  (see Table S3 in the supporting information).

## 5. Kinematic Indicators

Kinematic indicators were observed at both the outcrop and thin section scale across the full structural thickness of the Sarpang transect (Figure 3). They include SC fabrics (Figure 5f), rigid porphyroclasts sheared into  $\sigma$  objects (Figure 5g), C'-type shear bands (Figure 5h), asymmetric folds, asymmetric boudinage, rotated rigid clasts (Figure 5i), and mica fish. In addition, asymmetric quartz  $c$  axis fabrics [e.g., *Passchier and Trouw*,

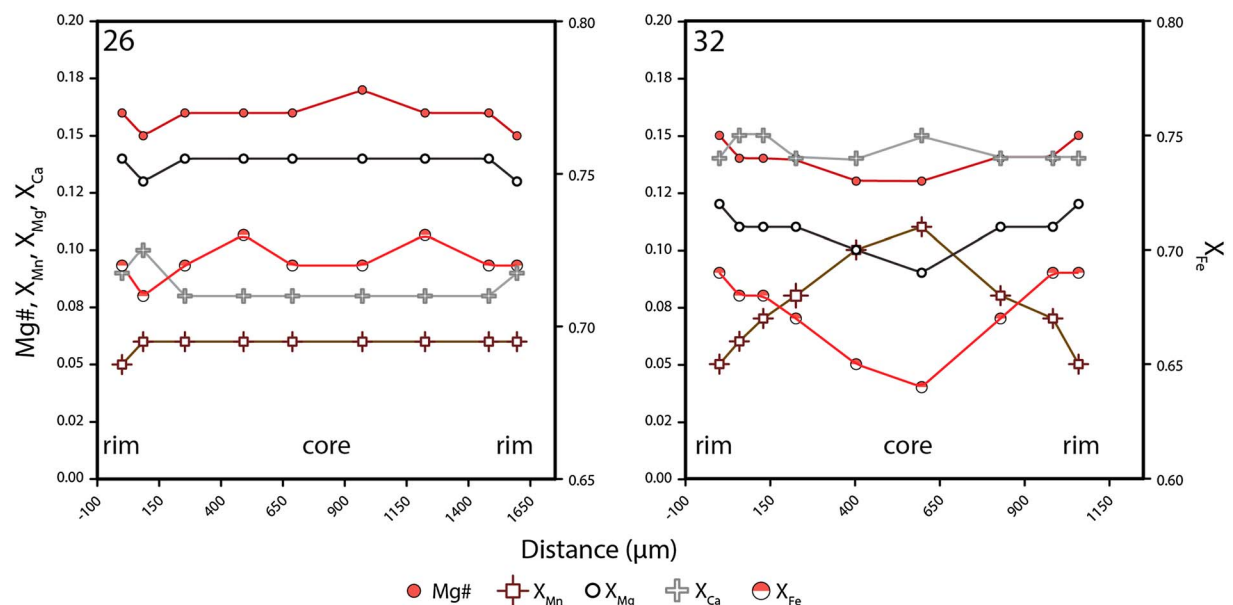


**Figure 9.** Quantitative element profiles of representative garnet from Jaishidanda Formation schist samples 26 and 32. The left axis represents the molar proportion of the Mg# ( $\text{Mg}/(\text{Mg} + \text{Fe})$ ) and three garnet end-members: grossular ( $X_{\text{Ca}}$ ), pyrope ( $X_{\text{Mg}}$ ), and spessartine ( $X_{\text{Mn}}$ ). The right axis represents the molar proportion of garnet end-member almandine ( $X_{\text{Fe}}$ ). The horizontal axis is the distance across the rim-to-rim transect.

**Table 3.** Summary of Finite Strain Data From Sarpang Transect Samples<sup>a</sup>

Thin Section	Map Unit	Lithology	Structural Height Relative to MCT (m)	Structural Height Relative to ST (m)	Foliation (d, dd)	Lineation (tr, pl)	Orientation Relative to Lineation	Thin Section Orientation (d, dd)	$R_s$ ( $\pm 1$ SE) <sup>b</sup>	$\phi$ (Equal to $\theta'$ ) ( $\pm 1$ SE)	$W_m$ Range From $R_s$ Versus $\theta'$ Method <sup>c</sup>	% Pure Shear From $R_s$ Versus $\theta'$ Method <sup>d</sup>	Quartz Porphyroblast Type <sup>e</sup>
19A	Daling	schist	-1025	1325	58, 025	56, 005	parallel	81, 289	4.2 $\pm$ 0.3	-3 $\pm$ 1°	0.20-0.30	80-85%	1
19B							perpendicular	33, 187	2.5 $\pm$ 0.1	7 $\pm$ 1°			
12A	Daling	quartzite	-2175	175	48, 335	46, 351	parallel	81, 072	3.3 $\pm$ 0.4	2 $\pm$ 1°	0.10-0.20	85-95%	3
12B							perpendicular	43, 168	2.5 $\pm$ 0.3	0 $\pm$ 2°			
11A	Daling	phyllite	-2300	50	60, 350	56, 018	parallel	75, 088	2.5 $\pm$ 0.1	-2 $\pm$ 1°	0.05-0.20	85-95%	1
11B							perpendicular	33, 200	1.9 $\pm$ 0.1	2 $\pm$ 2°			
9A	Manas	quartzite	-2425	-50	51, 330	30, 033	parallel	53, 098	2.1 $\pm$ 0.1	5 $\pm$ 2°	0.20-0.40	70-85%	3
9B							perpendicular	59, 212	1.9 $\pm$ 0.1	-1 $\pm$ 3°			
7A	Manas	quartzite	-2550	-200	50, 345	49, 002	parallel	81, 083	1.9 $\pm$ 0.1	-10 $\pm$ 2°	0.40-0.55	60-70%	3
7B							perpendicular	41, 180	1.9 $\pm$ 0.1	-3 $\pm$ 3°			
6A	Manas	quartzite	-3075	-725	22, 310	21, 325	parallel	84, 054	1.7 $\pm$ 0.1	-5 $\pm$ 2°	0.15-0.35	75-90%	2
6B							perpendicular	69, 146	1.6 $\pm$ 0.1	15 $\pm$ 3°			
5A	Manas	phyllite	-3375	-1025	31, 025	8, 307	parallel	60, 222	1.8 $\pm$ 0.1	-1 $\pm$ 2°	0.05-0.20	85-95%	1
5B							perpendicular	83, 118	1.2 $\pm$ 0.1	7 $\pm$ 7°			
4A	Manas	phyllite	-3575	-1225	36, 330	33, 356	parallel	77, 077	1.8 $\pm$ 0.1	-4 $\pm$ 2°	0.10-0.30	80-95%	1
4B							perpendicular	57, 174	1.8 $\pm$ 0.1	0 $\pm$ 3°			
3A	Manas	quartzite	-3725	-1375	29, 340	38, 357	parallel	89, 073	1.7 $\pm$ 0.1	-3 $\pm$ 2°	0.00-0.25	80-100%	2
3B							perpendicular	61, 175	1.5 $\pm$ 0.1	6 $\pm$ 3°			
2A	Manas	phyllite	-3925	-1575	9, 290	5, 346	parallel	82, 077	1.8 $\pm$ 0.1	-3 $\pm$ 2°	0.05-0.30	80-95%	1
2B							perpendicular	85, 166	1.5 $\pm$ 0.1	0 $\pm$ 2°			
1A	Manas	phyllite	-4425	-2075	32, 040	30, 020	parallel	78, 289	1.5 $\pm$ 0.1	-2 $\pm$ 4°	0.00-0.30	80-100%	1
1B							perpendicular	61, 193	1.5 $\pm$ 0.1	-3 $\pm$ 3°			

<sup>a</sup>d, dd = dip, dip direction notation, tr, pl = trend, plunge notation.  $R_s$  = tectonic elongation (long axis to short axis ratio),  $\phi$  = angle between long axis and foliation (equal to  $\theta'$  of Ramsay and Huber [1983]) (sign convention for  $\phi$ : clockwise from foliation is positive, counterclockwise from foliation is negative).  $W_m$  = mean kinematic vorticity number.

<sup>b</sup> $R_s$  values and associated errors are rounded to nearest 0.1.

<sup>c</sup>Estimated  $W_m$  values are rounded to nearest 0.05.

<sup>d</sup>Percent pure shear values were determined from Law *et al.* [2004] and are rounded to nearest 5%.

<sup>e</sup>Type 1: quartz porphyroclasts isolated within micaceous matrix; type 2: quartz porphyroclasts within clast-supported quartzite; type 3: quartz porphyroclasts isolated within matrix of quartz neoblasts.



2005] were observed in six EBSD samples (Figures 3 and 7). Samples 12A and 18A exhibit type II crossed girdles that are inclined relative to foliation, with 12A defining a top-to-north shear sense and 18A defining a top-to-south shear sense. Sample 21A has a type I crossed girdle, and samples 23A, 29A, and 31A have single girdles with the central section of the  $c$  axis fabric skeleton inclined relative to foliation, and all four define a top-to-south shear sense. Of the 18 total observed kinematic indicators and asymmetric quartz  $c$  axis fabrics, all but two (samples 22 and 12A) define a top-to-south shear sense (Figure 3). There were three instances where asymmetric  $c$  axis fabrics were obtained from samples collected at the same locality where thin section- or outcrop-scale kinematic indicators were observed (Figure 3). In two of these instances, the  $c$  axis fabrics and outcrop- or thin section-scale kinematic indicators both exhibited a top-to-south shear sense, and in one instance (samples 21A and 22), they yielded opposite shear senses.

## 6. Strain and Kinematic Vorticity Data

### 6.1. Three-dimensional Finite Strain of Quartz Porphyroclasts

Eight Manas Formation samples and three Daling Formation samples exhibit plastically elongated quartz porphyroclasts that have experienced minimal recrystallization (Figures 6a–6e). In order to quantify the magnitude and orientation of 3-D finite strain, the  $R_F\phi$  method [e.g., Ramsay, 1967; Dunnet, 1969; Dunnet and Siddons, 1971] was performed on quartz porphyroclasts in two foliation-normal thin sections from each sample, one parallel to lineation, which is interpreted to approximate the XZ strain plane and one normal to lineation, which is interpreted to approximate the YZ strain plane (details on methodology, representative photomicrographs, and data from individual analyses in the supporting information). Two-dimensional strain ellipses for individual samples are plotted in Figures 2 and 3, and data are summarized in Table 3. For all samples, the 2-D strain ratio ( $R_s$ ) in the lineation-parallel thin section was either greater than or equivalent within error to  $R_s$  in the lineation-normal thin section, and the direction of shortening in all thin sections was subnormal to foliation. This justifies the assumption that lineation and foliation can be used to approximate the principal strain directions within the studied rocks.

Strain ellipsoids for the Manas Formation samples are all quite similar, with X/Z ratios ranging between 1.5 and 2.1 and Y/Z ratios between 1.2 and 1.9. The mean X, Y, and Z elongation ratio for these samples is 1.75:1.55:1.00, which is similar to the 1.9:1.8:1.0 mean ratio calculated for Manas Formation samples in eastern Bhutan [Long et al., 2011c]. On a Flinn diagram, all but one of the Manas Formation strain ellipsoids plot in the apparent flattening field (Figure 10a).  $\phi$  angles were measured relative to foliation and are therefore equivalent to the parameter  $\theta'$ , defined as the acute angle between the grain long axis and foliation [e.g., Ramsay and Huber, 1983, p. 15] (for simplicity, from this point on,  $\phi$  is referred to as  $\theta'$ ). The sign convention used for  $\theta'$  is positive if down to the north or east relative to foliation and negative if down to the south or west relative to foliation. In both lineation-parallel and lineation-normal thin sections, mean  $\theta'$  values are quite low, with 14 of the 16 thin sections between  $\pm 7^\circ$ . There were two outlying values of  $-10^\circ$  and  $+15^\circ$ . In lineation-parallel thin sections, there is no consistent sense of obliquity exhibited by quartz porphyroclasts. The majority of samples exhibit  $\theta'$  values that either overlap within error with foliation or have error ranges that are within  $1-2^\circ$  of foliation (Figure 10b). The similar elongation magnitudes of the X and Y axes, combined with the low  $\theta'$  values, indicate that Manas Formation samples experienced layer-normal flattening (LNF) strain [e.g., Long et al., 2011c].

Strain ellipsoids from Daling Formation samples 11, 12, and 19, which are located 50 m, 175 m, and 1325 m above the ST, respectively (Figure 3), exhibit X/Z ratios that increase structurally upward from 2.5 to 4.2. The Y/Z ratios from these samples increase structurally upward from 1.9 to 2.5. The ellipsoids of all three samples plot in the apparent flattening field (Figure 10a). The XY strain plane is subparallel to foliation, with  $\theta'$  values between  $\pm 0$  and  $3^\circ$  and one outlying value of  $+7^\circ$ . Similar to the Manas Formation analyses, there is no consistent sense of obliquity exhibited by quartz porphyroclasts in the Daling Formation in lineation-parallel thin sections. All three samples have  $\theta'$  values with error ranges that are within  $1-2^\circ$  of foliation (Figure 10b). These data define LNF strain in the Daling Formation, with greater elongation magnitudes than the Manas Formation.

In addition, the two occurrences of top-to-north kinematic indicators on the Sarpang transect approximately coincide in structural position with Daling Formation samples that exhibit high X/Z ratios (Figure 3). This localized top-to-north shearing could be the result of higher lineation-parallel stretching at these structural positions compared to rocks above and below.

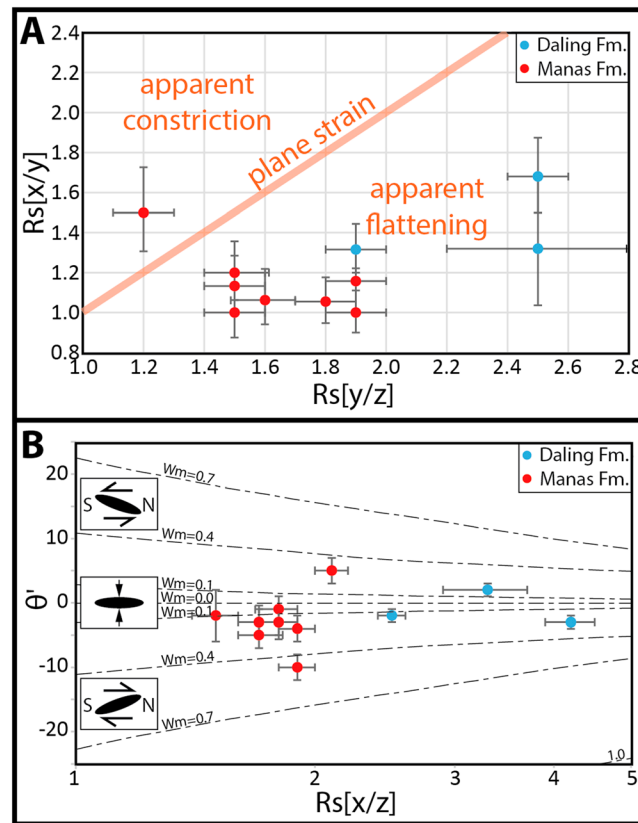


**Figure 10.** Finite strain data from  $R_F\text{-}\phi$  analyses of quartz porphyroclasts; all error bars are shown at 1 standard error. (a) Flinn diagram [e.g., Flinn, 1962] showing 3-D strain fields for constant-volume deformation. (b) Plot of tectonic elongation in lineation-parallel thin sections ( $R_s[X/Z]$ ) versus  $\theta'$  [e.g., Tikoff and Fossen, 1995]. Contours of mean kinematic vorticity for plane strain deformation ( $W_m$ ) are shown (modified from Yonkee [2005]).

## 6.2. Three-dimensional Incremental Strain of Quartz Neoblasts

Quartz neoblasts within the nine analyzed EBSD samples exhibit a shape-preferred elongation that is typically subparallel to foliation (Figure 7). Using a similar technique to the finite strain analyses, we performed  $R_F\text{-}\phi$  analyses on quartz neoblasts within lineation-parallel and lineation-normal thin sections (details on methodology, representative photomicrographs, and data from individual analyses in the supporting information). Unlike the finite strain analyses, these data are interpreted only to yield information on the magnitude of crystal-plastic strain that the sample has experienced since the final preserved dynamic recrystallization event (which assumes that the neoblasts initially formed approximately spherical). Alternatively, the data may record the strain field that the sample occupied during the final preserved dynamic recrystallization event (which assumes that the neoblasts recrystallized with the observed shape-preferred orientation). In either case, this data may be interpreted as quantifying incremental strain that

occurred either during or since the final preserved recrystallization event. Therefore, this data provides insight into the strain field at or after the time that the observed deformation fabrics were locked in [e.g., Law, 2014].

Two-dimensional strain ellipses for individual samples are plotted on Figure 3, and the data are summarized in Table 1. For all samples,  $R_s$  in the lineation-parallel thin section (XZ strain plane) was either greater than or equivalent within error to  $R_s$  in the lineation-normal thin section (YZ strain plane), and the direction of shortening (Z) was subnormal to foliation. In addition, all samples plot in the apparent flattening field (Figure 11a). The X/Z elongations range between 1.30 and 1.55, Y/Z elongations range between 1.25 and 1.45, and mean  $\theta'$  values in both the X and Y directions range between  $-5$  and  $+6^\circ$ , with two outlying values of  $-7^\circ$  and  $+9^\circ$ . There is no consistent sense of obliquity exhibited by quartz neoblasts in lineation-parallel thin sections; the majority of samples exhibit  $\theta'$  values that either overlap within error with foliation or have error ranges that are within  $1\text{--}2^\circ$  of foliation (Figure 11b). These data indicate that the samples occupied a LNF strain field during the final stages of recrystallization or along their exhumation path after recrystallization but before cooling through the  $\sim 250\text{--}270^\circ\text{C}$  minimum temperature range for quartz plasticity [e.g., Stipp et al., 2002].

As discussed above, these nine samples exhibit quartz fabrics that indicate approximate plane strain deformation [e.g., Schmid and Casey, 1986]. This contrasts with the incremental strain data, as all nine samples plot in the flattening field, and only two overlap within error with the plane strain line (Figure 11a). We interpret that the most likely cause of this disparity is that the majority of the flattening strain that we document in quartz neoblasts likely postdates the accumulation of quartz crystallographic fabrics in these samples. Therefore, the strain path of these quartz-rich rocks may have progressed from approximately plane strain conditions during high-temperature shearing to a flattening-dominated field further along their exhumation path.

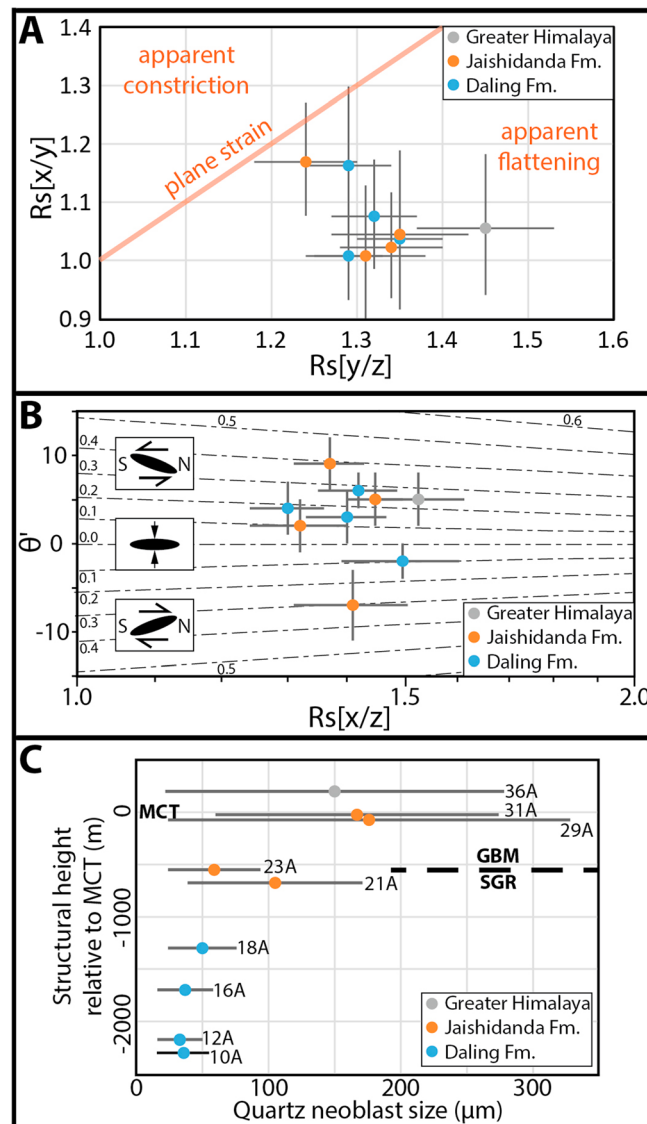


**Figure 11.** Incremental strain data from  $R_F\phi$  analyses of quartz neoblasts. (a) Flinn diagram [e.g., Flinn, 1962], showing 3-D strain fields for constant-volume deformation. Error bars are shown at 1 standard error. (b) Plot of tectonic elongation in lineation-parallel thin sections ( $R_s[x/z]$ ) versus  $\theta'$  [e.g., Tikoff and Fossen, 1995], with contours of mean kinematic vorticity for plane strain deformation ( $W_m$ ) plotted. Error bars are shown at 1 standard error. (c) Graph of quartz neoblast size in lineation-parallel thin sections versus structural height for the nine incremental strain samples. Error is shown at  $1\sigma$  level.

date the accumulation of quartz crystallographic fabrics. Therefore, the measured  $\beta$  and  $\theta'_{ISA1}$  angles may record earlier and later portions of the strain history, respectively. Thus, interpretation of  $W_m$  values obtained from the quartz shape-preferred orientation method requires assuming that the measured  $\theta'_{ISA1}$  was at a similar angle to foliation during the accumulation of quartz fabrics [e.g., Johnson et al., 2009; Law, 2010]. In the  $R_s\text{-}\theta'$  method,  $R_s[x/z]$  and  $\theta'$  values from finite and incremental strain analyses were plotted and compared to graphed curves of constant  $W_m$  value (Figures 10b and 11b) [e.g., Tikoff and Fossen, 1995; Yonkee, 2005]. For both methods of vorticity analysis, the simplified case of steady state plane strain is assumed for estimation of  $W_m$  [e.g., Fossen and Tikoff, 1993; Johnson et al., 2009]. However, since the rocks that we analyzed experienced flattening strain, the resulting  $W_m$  values are interpreted to represent maxima [Tikoff and Fossen, 1995]. Given the relatively low strain magnitudes of our samples ( $R_s \sim 1.5\text{--}4$ ), the overestimation of

### 6.3. Estimation of Mean Kinematic Vorticity

The kinematic vorticity number is a dimensionless ratio that quantifies the relative contributions of pure shear and simple shear [e.g., Means et al., 1980; Passchier, 1987; Tikoff and Fossen, 1993; Means, 1994]. Passchier [1987] suggested that the kinematic vorticity number extracted from rocks be called the mean kinematic vorticity number ( $W_m$ ); therefore, we express our results in terms of  $W_m$ . A  $W_m$  value of 0 represents idealized pure shear, a value of 1 represents idealized simple shear, and equal contributions occur at  $W_m = 0.71$  [Law et al., 2004]. We estimated  $W_m$  within lineation-parallel (X/Z) thin sections using the quartz shape-preferred orientation method of Wallis [1992, 1995] and by comparing our data to  $W_m$  curves plotted on a graph of  $R_s$  versus  $\theta'$  (referred to here as the  $R_s\text{-}\theta'$  method) [e.g., Tikoff and Fossen, 1995].

The quartz shape-preferred orientation method estimates  $W_m$  through measurement of two angles:  $\beta$ , the angle between foliation and the line normal to the central girdle segment of a quartz  $c$  axis fabric skeleton (Figure 7), and  $\theta'_{ISA1}$ , the mean  $\theta'$  angle from a data set of  $\geq 100$  measured quartz neoblasts (supporting data and additional details on methodology in the supporting information). As discussed above, the flattening strain documented in quartz neoblasts represents the final preserved increment of plastic deformation in these rocks and may post-

$W_m$  introduced by assuming plane strain likely does not exceed  $\sim 0.05$  [Tikoff and Fossen, 1995]. The range of  $W_m$  values reported for each sample is estimated from the  $\pm 1$  standard error reported for the mean  $\theta'$  value of each sample. All  $W_m$  ranges are rounded to the nearest 0.05, and corresponding contributions of pure and simple shear [from Law *et al.*, 2004] are rounded to the nearest 5%.

For the 11 finite strain samples of the Manas and Daling Formations, the  $R_s$ - $\theta'$  method yielded  $W_m$  values typically between 0.00 and 0.30 (80–100% pure shear) (Figure 10b and Table 3); one sample (7) yielded an outlying  $W_m$  range of 0.40–0.55 (60–70% pure shear). For the nine incremental strain samples from the Daling Formation, Jaishidanda Formation, and GH section, the  $R_s$ - $\theta'$  method yielded  $W_m$  values typically between 0.00 and 0.35 (75–100% pure shear) (Figure 11b and Table 1). Two samples (29A, 31A) had outlying values as high as 0.45–0.50 (65% pure shear). The quartz shape-preferred orientation method was performed on eight of these samples and yielded values typically between 0.00 and 0.35 (75–100% pure shear) (Table 1); one sample (31A) yielded an outlying value of 0.45–0.65 (55–70% pure shear).

The  $W_m$  values from the Sarpang transect can be compared to published vorticity data from transects across the MCT along strike in the Himalaya. Jessup *et al.* [2006] obtained  $W_m$  numbers between 0.60 and 0.77 (45–60% pure shear;  $n=8$ ) across the MCT in eastern Nepal, and Grasemann *et al.* [1999] and Law *et al.* [2013] obtained  $W_m$  numbers between 0.57–0.71 (50–60% pure shear;  $n=33$ ) and 0.73–1.00 (0–45% pure shear;  $n=21$ ), respectively, across the MCT in northwest India. Therefore, in comparison to these data from the central and western Himalaya, the vorticity data from the Sarpang transect indicate a more significant component of pure shear. The low  $W_m$  values obtained on the Sarpang transect are similar to those obtained above and below the MCT in eastern and central Bhutan. Long *et al.* [2011c], using the  $R_s$ - $\theta'$  method, determined  $W_m$  values from the Manas Formation ( $n=41$ ) and from GH and Tethyan Himalayan rocks ( $n=37$ ). The  $W_m$  values yielded a total range between 0.0 and 1.0, but the majority of samples ( $n=55$ ) yielded values  $< 0.7$ , and nearly half ( $n=34$ ) yielded values  $< 0.4$ .

## 7. Discussion

### 7.1. Calculation of Thermal Field Gradients

The four temperature data sets are in good agreement (Figures 3 and 12a). Techniques that semiquantitatively bracket (quartz recrystallization mechanisms) and quantify (quartz fabric opening angles) deformation temperature yielded results that overlap with error with techniques that quantify peak temperature (RSCM, garnet-biotite thermometry). Therefore, we interpret that the observed quartz fabrics were locked in while the studied rocks were at or near peak temperature [e.g., Law, 2014]. The quantitative peak and deformation temperature data sets were therefore grouped together to define thermal field gradients. The transect can be divided into two sections that exhibit inverted field gradients, which overlap with the mapped positions of the ST and MCT (Figure 12a) and are separated by sections in which temperatures remain essentially constant. From structurally-lowest to highest, these sections are:

1. The Manas Formation sheet (2075–1225 m below the ST; samples 1A, 3A, and 4A): RSCM temperatures overlap within error, between  $\sim 300$  and  $400^\circ\text{C}$ .
2. The ST inverted gradient, which is supported by sample 4A (1225 m below the ST) and samples 10A and 11A (50 m above the ST) (Figure 12a). Temperatures increase from  $353 \pm 61^\circ\text{C}$  (sample 4A) to  $397$ – $535^\circ\text{C}$  (the total temperature range from samples 10A and 11A) and are best fit by a thermal field gradient of  $72 \pm 51^\circ\text{C/km}$  ( $2\sigma$ , mean square weighted deviation (MSWD) = 3.7, probability = 0.054; calculated from a linear regression using IsoPlot v. 4.15 [Ludwig, 2008], using an uncertainty of  $\pm 50$  m for structural height). The broad error ranges on the quantitative temperatures determined for samples in this interval bracket a wide permissible field gradient range. Also, because of the 1275 m thick data gap between samples 4A and 10A–11A, the calculated field gradient is interpreted as an approximate, minimum estimate.
3. The ST sheet (50–1675 m above the ST; 2300–675 m below the MCT; samples 10A–21A): temperatures overlap within error, and range between  $\sim 400$  and  $550^\circ\text{C}$ .
4. The MCT inverted gradient (675 m below to 200 m above the MCT), which is supported by temperatures from nine samples (21A–36A; Figure 12a). Collectively, temperatures increase from  $455 \pm 50^\circ\text{C}$  to  $719 \pm 27^\circ\text{C}$  and are best fit by a thermal field gradient of  $269 \pm 44^\circ\text{C/km}$  ( $2\sigma$ , MSWD = 1.3, probability = 0.22; calculated using the same method described above for the ST field gradient). In comparison, temperatures collected from GH rocks in transects 35 and 60 km to the east show that maximum temperatures



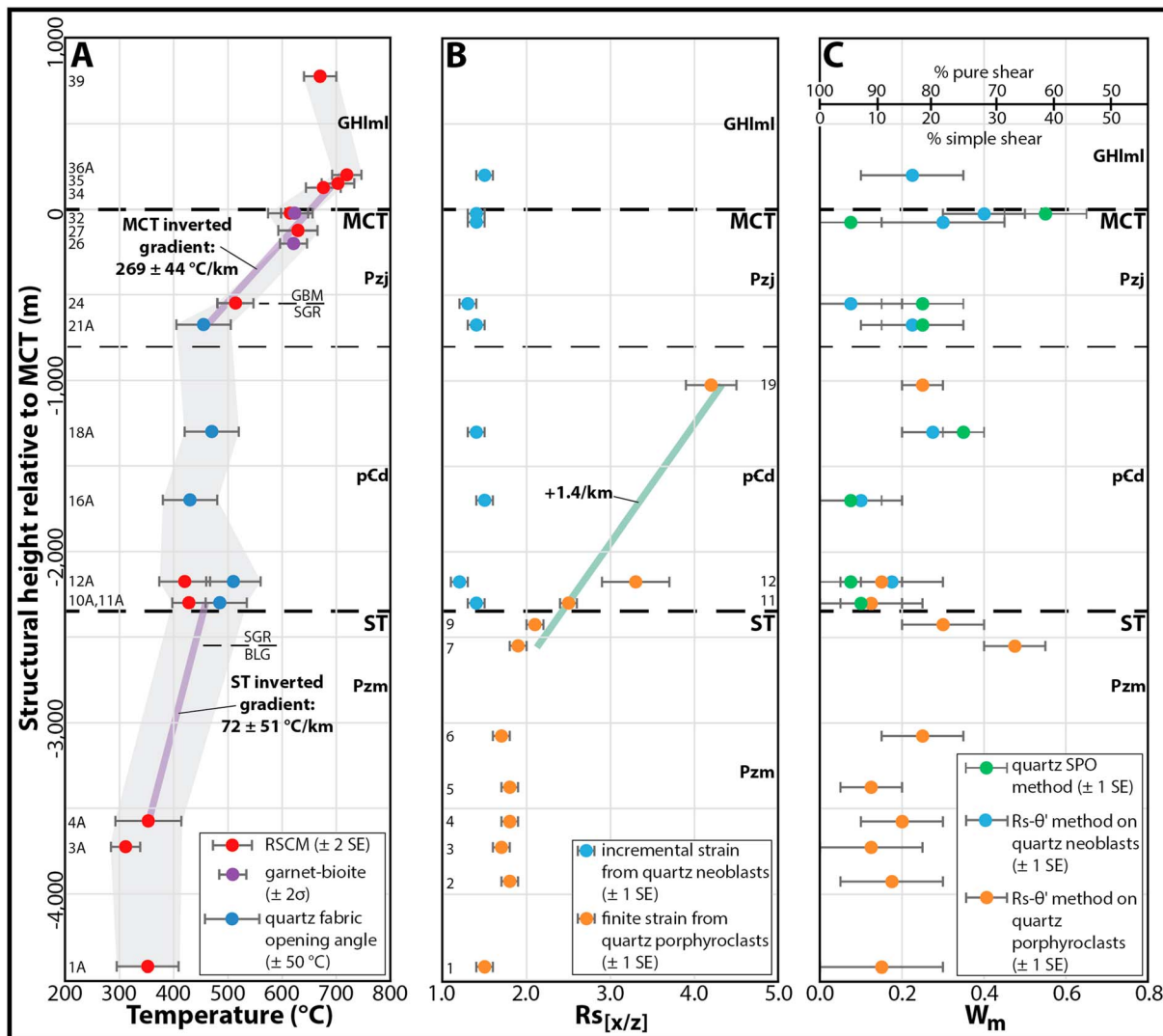


**Figure 12.** Graphs of (a) temperature, (b) tectonic elongation in lineation-parallel thin sections ( $R_{s[x/z]}$ ), and (c) mean kinematic vorticity number ( $W_m$ ) versus structural height relative to the MCT. ST, Shumar thrust; MCT, Main Central thrust; SE, standard error. See Figure 2 for explanation of rock unit abbreviations and Figure 3 for explanation of quartz recrystallization mechanism abbreviations.

of ~660–725°C were obtained 100–125 m above the MCT and systematically decrease structurally upward at a rate of  $20 \pm 2^\circ\text{C}/\text{km}$  [Corrie *et al.*, 2012]. This indicates that the full structural thickness of inverted metamorphism across the MCT is captured on the Sarpang transect.

5. The basal part of the MCT sheet (200–775 m above the MCT): temperatures from samples 36A and 39 overlap within error, at  $719 \pm 27^\circ\text{C}$  and  $670 \pm 30^\circ\text{C}$ , respectively.

## 7.2. Interpretation of Main Central Thrust Thermal Field Gradient

Temperatures from the Sarpang transect add to a body of studies that quantify inverted metamorphic field gradients across the MCT (see recent reviews in Law *et al.* [2013], Law [2014], and Kohn [2014]). In northwest India and western Nepal, deformation temperatures from quartz *c* axis opening angles are typically ~450–550°C as the MCT is crossed and increase structurally upward to ~600–650°C, with linear, best fit field gradients as high as ~90–100°C/km reported [Law *et al.*, 2013, and references therein]. In comparison, compilations of peak metamorphic temperatures from transects across the MCT that span the width of the orogen illustrate similar increases from ~550°C in LH rocks to ~700–800°C in GH rocks [Kohn, 2014]. The difference between the deformation and metamorphic temperature ranges compiled in these studies is attributed to differences in the interpreted structural position of the MCT. Law *et al.* [2013] and Law [2014] define the MCT at a structurally

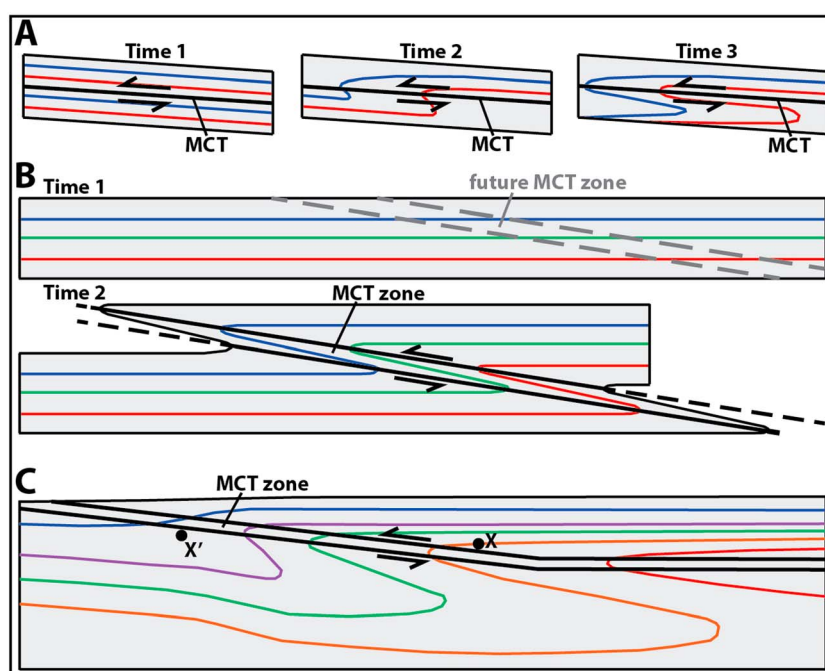


**Figure 13.** Diagrams illustrating three scenarios proposed for MCT inverted metamorphism. (a) Downward heat conduction ("hot iron effect" of *LeFort* [1975]) over duration of MCT motion. (b) Postmetamorphic, distributed shearing of originally flat, upright isograds [e.g., *Grujic et al.*, 1996] within MCT zone. (c) Long-distance structural transport through thermal regime of sigmoidally folded isotherms produced from protracted continental underthrusting [e.g., *Royden*, 1993; *Henry et al.*, 1997; *Kohn*, 2014]. With significant displacement, points X and X' will be juxtaposed across the MCT zone (modified from *Kohn* [2014]).

lower position in the thrust belt, after criteria defined in *Searle et al.* [2008], whereas *Kohn* [2014] defines the MCT at a structurally higher position, after earlier mapping [e.g., *LeFort*, 1975; *Pecher*, 1989].

The structural position of the MCT as mapped in our study is similar to that of *Kohn* [2014], which allows direct comparison with his temperature compilations. In northwest India, western Nepal, and eastern Nepal/Sikkim, inverted metamorphism is distributed from as low as 2–3 km below to as high as 3–7 km above the MCT, corresponding to best fit inverted field gradients of  $\sim 20\text{--}40^\circ\text{C/km}$  (calculated from *Kohn* [2014, Figure 4]). In comparison, the inverted gradient across the MCT that we document on the Sarpang transect is much steeper at  $269 \pm 44^\circ\text{C/km}$ , the steepest thus far documented in the Himalaya. In addition, the Sarpang thermal field gradient is steeper than the  $\sim 100\text{--}160^\circ\text{C/km}$  inverted gradient across the MCT (calculated from *Jamieson et al.* [2004, Figure 8]) predicted by a thermal-mechanical orogenic model based on Himalayan parameters [*Beaumont et al.*, 2004; *Jamieson et al.*, 2004].

Multiple processes have been proposed for the origin of inverted metamorphism across the MCT. *LeFort* [1975] interpreted that downward heat conduction associated with emplacement of hot GH rocks produced the inversion (Figure 13a). Other studies have proposed postmetamorphic, distributed shearing of originally flat, upright isotherms (Figure 13b) [*Grujic et al.*, 1996; *Vannay and Grasemann*, 2001]. Alternatively, inverted metamorphism could be achieved through long-distance structural transport through a thermal regime of sigmoidally folded isotherms produced during protracted continental underthrusting (Figure 13c) [*Royden*, 1993; *Henry et al.*, 1997; *Kohn*, 2014].

The observed steepness and thickness of the MCT inverted gradient on the Sarpang transect can be used to test the conductive heating scenario. Thermal equilibration of the MCT footwall, and the corresponding steepness and thickness of the inverted thermal gradient, can be modeled as a function of temperature difference, thermal diffusivity, and equilibration time [*Turcotte and Schubert*, 2002, equations (4)–(113)]. Input parameters were  $250^\circ\text{C}$  for temperature difference and  $8.6 \times 10^{-7} \text{ m}^2/\text{s}$  for thermal diffusivity (obtained from the average of values for orthogneiss, gneiss, schist, and sandstone in *Eppelbaum et al.* [2014]). To reproduce the inverted field gradient observed on the Sarpang transect ( $269 \pm 44^\circ\text{C/km}$  over a vertical thickness of 875 m)

would require thermal equilibration over a (geologically) near-instantaneous timescale of 1 Kyr. In comparison, equilibration over 10 Kyr yields an  $\sim 83^{\circ}\text{C}/\text{km}$  gradient distributed through  $\sim 3$  km, 100 Kyr yields an  $\sim 25^{\circ}\text{C}/\text{km}$  gradient distributed through  $\sim 10$  km, and 1 Myr yields an  $\sim 8.3^{\circ}\text{C}/\text{km}$  gradient distributed through  $\sim 30$  km. MCT motion in Bhutan likely occurred over 6–7 Myr (23–16 Ma in eastern Bhutan, 21–15 Ma in western Bhutan) [Daniel *et al.*, 2003; Chambers *et al.*, 2011; Long *et al.*, 2012; Tobgay *et al.*, 2012]. Even using a conservative duration estimate of 1 Myr, the gradient observed on the Sarpang transect is only reproducible with conductive heating if structural thinning accompanying shearing within the MCT zone approached a factor of 30. There is evidence for structural thinning of LH rocks as shallow as 1 km below the MCT and in GH rocks between 0.1 and 6 km above the MCT; however, it is on the order of 40–50% [Long *et al.*, 2011c; Corrie *et al.*, 2012; this study]. Therefore, the steep MCT gradient on the Sarpang transect is not reproducible under a scenario dominated by conductive heating.

The scenarios of distributed shearing of upright, flat isotherms (Figure 13b) [e.g., Grujic *et al.*, 1996] and long-distance transport through folded isotherms (Figure 13c) [e.g., Kohn, 2014] cannot be unequivocally discerned with our data. However, under both scenarios, the upper and lower bounds of inverted metamorphism are predicted to delineate the approximate top and bottom of a zone of high-magnitude, differential southward translation. Therefore, the 875 m thick interval of rock that contains the steep MCT inverted gradient on the Sarpang transect is interpreted to bracket the boundaries of a high-offset “MCT zone.” This defines the MCT as a relatively discrete shear zone within the overall 35–60 km minimum structural thickness of the Himalayan thrust belt in Bhutan [Long *et al.*, 2011b].

Under both scenarios, the magnitude of inverted temperature difference is broadly proportional to transport distance [e.g., Kohn, 2008, 2014]. For the scenario of long-distance structural transport through folded isotherms, thermal models of the Himalayan orogen facilitate estimation of MCT offset magnitude on the basis of inverted temperature difference [e.g., Kohn *et al.*, 2004; Corrie and Kohn, 2011]. On the “hot” and “cold” end-member thermal models of Corrie and Kohn [2011, Figure 7], south to north gradients of  $\sim 2.5^{\circ}\text{C}/\text{km}$  and  $\sim 1^{\circ}\text{C}/\text{km}$ , respectively, can be estimated along the Main Himalayan thrust between the 500 and 800°C isotherms. Assuming that major, in-sequence Himalayan shear zones such as the MCT occupied the position of the Main Himalayan thrust when they were active [e.g., Bollinger *et al.*, 2004; Corrie and Kohn, 2011; Kohn, 2014; Larson and Cottle, 2014; Larson *et al.*, 2015], these thermal models estimate a  $\sim 100$ –250 km range of offset for the MCT on the Sarpang transect. These estimates can be interpreted as approximate lower and upper bounds and are compatible with 100–175 km estimates of minimum structural overlap on the MCT on Bhutan cross sections [Long *et al.*, 2011b; Tobgay *et al.*, 2012].

### 7.3. Interpretation of Shumar Thrust Thermal Field Gradient

In comparison to the MCT, the magnitude and thickness of inverted metamorphism across the ST is not as tightly constrained. The  $72 \pm 51^{\circ}\text{C}/\text{km}$  field gradient calculated above is interpreted as an approximate, minimum estimate. Because of the 1275 m data gap between samples that yielded quantitative temperatures, it is difficult to precisely estimate the depth beneath the ST at which deformation temperature conditions begin to increase. Sample 7 (200 m below the ST), which records the structural position of the BLG-SGR transition, represents the lowest microstructural evidence for increasing deformation temperature conditions. Finite strain magnitudes are approximately static through the Manas Formation sheet but show a slight increase between 200 and 50 m below the ST (Figure 12b). Also, an upsection transition from 30% to 80–100% quartz recrystallization is observed between 200 and 50 m below the ST. After these structural observations, we interpret that the ST is a discrete, south vergent shear zone, which affected an interval of rock perhaps as thin as  $\sim 200$  m below its mapped position.

The increase in temperatures across the ST is attributed to structural juxtaposition of rocks that experienced different peak burial depths prior to exhumation; i.e., the Daling Formation in the ST hanging wall experienced deeper burial and higher temperature conditions than the Manas Formation in the ST footwall [e.g., Long *et al.*, 2011c]. This is supported by the approximately static “background” temperatures of  $\sim 300$ –400°C distributed through much of the Manas Formation sheet and  $\sim 400$ –550°C distributed through much of the ST sheet.

Similar to the MCT, an approximate offset range for the ST can be estimated using the magnitude of inverted metamorphism. On the hot and cold Himalayan thermal models of Corrie and Kohn [2011, Figure 7], a



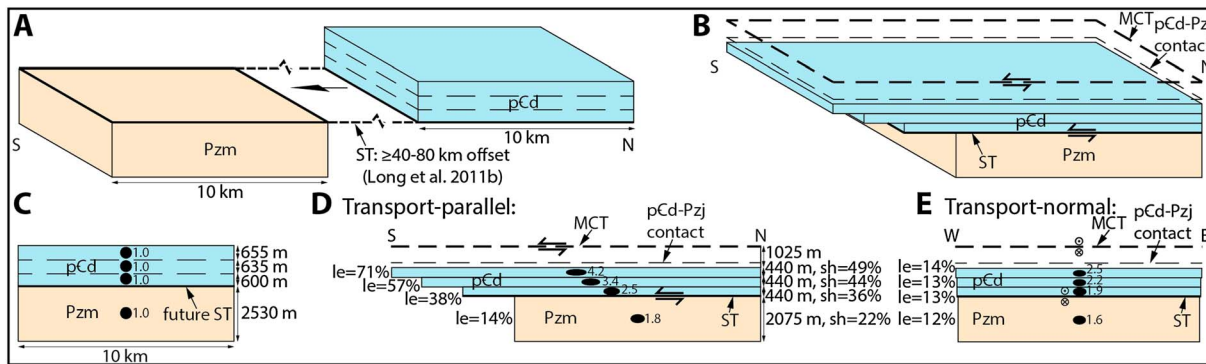


**Figure 14.** Block diagrams illustrating the change in dimensions of a 10 km × 10 km area of the Manas Formation (Pzm) sheet and Daling Formation (pCd) in the ST sheet, before and after observed finite strain (assuming homogeneous LNF strain across and along strike). (a and b) Before and after 3-D diagrams. (c, d, and e) Two-dimensional diagrams, showing (c) original width, thicknesses, and undeformed strain ellipses, and final thicknesses, deformed lengths, strain ellipses, and lengthening (le) and shortening (sh) values in (d) transport-parallel and (e) transport-normal view planes. The Daling Formation is simplified into three boxes; the bottom and top boxes illustrate strain ratios and lengthening and shortening values from samples 11 and 19, respectively, and the middle box represents a linear interpolation between these values.

south-to-north gradient range of 3–4°C/km can be estimated along the Main Himalayan thrust between the 300°C and 500°C isotherms. This corresponds to a maximum permissible offset range of ~60–85 km, which is similar to the 40–80 km range of structural overlap measured for the ST in cross sections of eastern Bhutan [Long *et al.*, 2011b].

#### 7.4. Structural Significance of Strain and Vorticity Data

Comparison of strain and vorticity data with structural distance allows estimation of field gradients within LH thrust sheets. Here these data are discussed from structurally lowest to highest positions.

Within the Manas Formation, finite strain magnitudes and kinematic vorticity numbers remain essentially constant with varying structural position (Figures 12b and 12c). Samples 1–7 yield similar LNF strain ellipsoids, with average  $X/Z$  and  $Y/Z$  ratios of 1.75 and 1.55 and yield typical  $W_m$  values of 0.1–0.3. Using this average ellipsoid (1.75:1.55:1.00), and using methods outlined in Wallis *et al.* [1993] and Law [2010], which incorporate strain magnitude and vorticity to calculate lengthening and shortening (all lengthening and shortening values listed below were calculated using these methods), a transport-parallel lengthening of 14%, a transport-normal lengthening of 12%, and 22% foliation-normal shortening is calculated for the Manas Formation sheet (Figure 14). Similar LNF strain magnitudes were documented in the Manas Formation in eastern Bhutan [Long *et al.*, 2011c]. After Long *et al.* [2011c], LNF strain accommodated within the Manas Formation on the Sarpang transect is interpreted to have accompanied tectonic burial during motion on the ST.

Sample 9, located 50 m below the ST, yielded slightly higher strain values (20% transport-parallel lengthening, 16% transport-normal lengthening, and 26% foliation-normal shortening) in comparison to other Manas Formation samples and marks the beginning of a structurally upward trend in increasing finite strain magnitude (Figure 12b). Within the ST sheet, strain ellipsoids from Daling Formation samples 11, 12, and 19 yielded increasing transport-parallel lengthening values of 38%, 46%, and 71%, transport-normal lengthening values of 13%, 24%, and 14%, and increasing foliation-normal shortening values of 36%, 44%, and 49%, respectively (Figure 14). Comparison of transport-parallel lengthening between samples 11 and 19 indicates an increasing lengthening gradient of 26% per kilometer through the lower half of the ST sheet, which imparts an overall top-to-south shear strain within the ST sheet. Assuming that LNF strain magnitudes are similar across strike, this corresponds to a differential southward transport distance between the base and middle of the ST sheet equal to 33% of the N-S length of Daling Formation rocks involved in deformation. Restored, minimum N-S length estimates of the Daling Formation in cross sections across Bhutan and Sikkim are typically between 130 and 150 km [Long *et al.*, 2011b; Tobgay *et al.*, 2012; McQuarrie *et al.*, 2014; Bhattacharyya *et al.*, 2015]. Using the 33% estimate for the Sarpang transect, this corresponds to a 43–50 km difference in southward translation distance between the base and middle of the ST sheet. This demonstrates that gradients in transport-parallel stretching accommodated within rocks between first-order shear zones can make a significant contribution to cumulative

southward transport [e.g., *Grujic et al.*, 1996; *Grasemann et al.*, 1999; *Vannay and Grasemann*, 2001; *Law et al.*, 2004, 2011, 2013]. This stretching gradient enhances southward transport distance in addition to the minimum across-strike structural overlap on the MCT, which ranges between 100 and 175 km on Bhutan cross sections [*Long et al.*, 2011b; *Tobgay et al.*, 2012]. Also, assuming that LNF magnitudes are similar across strike, southward translation distance at any given structural level must increase exponentially toward the foreland, as a condition of strain compatibility [e.g., *Williams et al.*, 2006; *Law et al.*, 2011].

Above sample 19 (1025 m below the MCT), finite strain magnitudes in Jaishidanda Formation and GH samples could not be quantified. However, incremental strain analyses and typical  $W_m$  values of 0.0–0.3 through this interval of rock all indicate a similar, pure shear-dominated LNF strain field during or after the final episode of quartz recrystallization (Figure 12c). Above the MCT, along a transect 40 km to the east, *Long et al.* [2011c] documented LNF strain and an increase in finite strain magnitude as the MCT is approached from above. Tethyan Himalayan rocks between 6 and 9 km above the MCT yielded an average strain ellipsoid of 2.10:1.70:1.00 and an average  $W_m$  value of 0.45 ( $n = 19$ ) [*Long et al.*, 2011c], corresponding to 13% transport-parallel lengthening, 11% transport-normal lengthening, and 20% foliation-normal shortening. GH rocks between 2.5 and 6 km above the MCT yielded an average strain ellipsoid of 3.65:2.15:1.00 and an average  $W_m$  value of 0.35 ( $n = 22$ ) [*Long et al.*, 2011c], corresponding to 61% transport-parallel lengthening, 8% transport-normal lengthening, and 42% foliation-normal shortening. These data are supported by a superlithostatic pressure gradient obtained through GH and Tethyan Himalayan rocks between 0.1 and 9 km above the MCT, which was interpreted to record ~50% bulk flattening of the section [*Corrie et al.*, 2012].

Based on these new data, internal strain above and below the MCT was dominated by layer-parallel stretching and layer-normal shortening, with magnitudes of both increasing with proximity to the MCT. This indicates that the MCT is a “stretching fault” [*Means*, 1989], on which translation on the order of hundreds of kilometers was accompanied by transport-parallel lengthening of hanging wall and footwall rocks on the order of tens of kilometers.

## 8. Conclusions

1. Temperatures of deformation and metamorphism estimated for LH and GH rocks in south central Bhutan define inverted field gradients across the MCT and ST, which are separated by sections in which temperatures remain essentially constant. Temperatures increase from ~400–500°C to ~700–750°C between 675 m below and 200 m above the MCT, defining a  $269 \pm 44^\circ\text{C}/\text{km}$  gradient, the steepest thus far documented in the Himalaya. Temperatures increase from ~300–400°C to ~400–530°C between 1225 m below and 50 m above the ST.
2. The steep inverted gradient across the MCT is interpreted to have formed as a result of high-magnitude (~100–250 km), south vergent shearing on a single, discrete shear zone, with its upper and lower bounds delineated by the 875 m thick interval of inverted metamorphism. This defines the MCT as a relatively discrete shear zone within the >35–60 km thick Bhutan thrust belt.
3. The inverted field gradient across the ST cannot be precisely estimated. However, microstructural observations indicate that the ST is a discrete (perhaps as thin as ~200 m) shear zone. The temperature increase across the ST is attributed to emplacement of hanging wall rocks that were buried to and deformed at higher temperatures than rocks in the footwall.
4. LH thrust sheets were deformed by pure shear-dominated ( $W_m$  ~0.0–0.3) LNF strain. Rocks below the ST experienced 14% transport-parallel lengthening and 22% foliation-normal shortening. Above the ST, transport-parallel lengthening and foliation-normal shortening increase from 38–71% to 36–49%, respectively, between 2.3 and 1.0 km below the MCT. Finite strain magnitudes could not be quantified between 1.0 km below and 0.8 km above the MCT; however, incremental strain data and  $W_m$  values of ~0.0–0.3 through this interval indicate pure-shear dominated LNF strain during or after the final episode of quartz recrystallization.
5. The MCT in southern Bhutan acted as a stretching fault, with translation on the order of hundreds of kilometers accompanied by transport-parallel stretching of hanging wall and footwall rocks on the order of tens of kilometers. This demonstrates that layer-parallel stretching accommodated in rocks between first-order shear zones can make a significant contribution to cumulative mass transfer.

## Acknowledgments

We would like to thank the government of Bhutan for their support, in particular Tashi Tenzin, Yonten Phuntsho, and Chief Geologist/Head Ugyen Wangda of the Department of Geology and Mines in the Ministry of Economic Affairs. We are indebted to Owen Neill at the WSU School of the Environment Analytical Laboratory and Pui Ching Wo and David Field at the WSU School of Mechanical and Materials Engineering FESEM laboratory. Conversations with Matt Kohn and Katie Cooper contributed to several ideas presented here. Constructive reviews by Richard Law, Kyle Larson, and associate editor John Cottle significantly improved this manuscript. This work was funded by NSF EAR-1220300 awarded to S. Long and S. Gordon. All data used for this research are included in the manuscript and supporting information.

## References

- Allmendinger, R. W., N. Cardozo, and D. Fisher (2011), *Structural Geology Algorithms: Vectors and Tensors in Structural Geology*, pp. 304, Cambridge Univ. Press, New York.
- Aoya, M., Y. Kouketsu, S. Endo, H. Shimizu, T. Mizukami, D. Nakamura, and S. Wallis (2010), Extending the applicability of the Raman carbonaceous-material geothermometer using data from contact metamorphic rocks, *J. Metamorph. Geol.*, **28**, 895–914, doi:10.1111/j.1525-1314.2010.00896.x.
- Bailey, J. E., and P. B. Hirsch (1962), The recrystallization process in some polycrystalline metals, *Proc. R. Soc. Lond.*, **A267**, 11–30.
- Beaumont, C., R. A. Jamieson, M. H. Nguyen, and B. Lee (2001), Himalayan tectonics explained by extrusion of a low-viscosity crustal channel coupled to focused surface denudation, *Nature*, **414**, 738–742.
- Beaumont, C., R. A. Jamieson, M. H. Nguyen, and S. Medvedev (2004), Crustal channel flows: 1. Numerical models with applications to the tectonics of the Himalayan-Tibetan orogen, *J. Geophys. Res.*, **109**, B06406, doi:10.1029/2003JB002809.
- Beyssac, O., B. Goffe, C. Chopin, and J. Rouzaud (2002), Raman spectra of carbonaceous material in metasediments: A new geothermometer, *J. Metamorph. Geol.*, **20**, 859–871, doi:10.1046/j.1525-1314.2002.00408.x.
- Beyssac, O., B. Goffe, J. P. Petit, E. Froigneux, M. Moreau, and J. N. Rouzaud (2003), On the characterization of disordered and heterogeneous carbonaceous materials by Raman spectroscopy, *Spectrochim. Acta, Part A*, **59**, 2267–2276, doi:10.1016/S1386-1425(03)00070-2.
- Bhargava, O. N. (1995), *The Bhutan Himalaya: A Geological Account*, vol. 39, pp. 245, Spec. Publ. Ser. Geol. Surv., India.
- Bhattacharyya, K., G. Mitra, and S. Kwon (2015), Geometry and kinematics of the Darjeeling–Sikkim Himalaya, India: Implications for the evolution of the Himalayan fold-thrust belt, *J. Asian Earth Sci.*, **113**, 778–796, doi:10.1016/j.jseas.2015.09.008.
- Blumenfeld, P., D. Mainprice, and J. L. Bouchez (1986), C-slip in quartz from subsolidus deformed granite, *Tectonophysics*, **27**, 271–294.
- Bollinger, L., J. P. Avouac, O. Beyssac, E. J. Catlos, T. M. Harrison, M. Grove, B. Goffe, and S. Sapkota (2004), Thermal structure and exhumation history of the Lesser Himalaya in central Nepal, *Tectonics*, **23**, TC5015, doi:10.1029/2003TC001564.
- Catlos, E. J., T. M. Harrison, M. J. Kohn, M. Grove, F. J. Ryerson, C. E. Manning, and B. N. Upreti (2001), Geochronologic and thermobarometric constraints on the evolution of the Main Central Thrust, central Nepal Himalaya, *J. Geophys. Res.*, **106**, 16,177–16,204, doi:10.1029/2000JB900375.
- Cawood, P. A., M. R. W. Johnson, and A. A. Nemchin (2007), Early Paleozoic orogenesis along the Indian margin of Gondwana: Tectonic response to Gondwana assembly, *Earth Planet. Sci. Lett.*, **255**, 70–84.
- Chambers, J., R. Parrish, T. Argles, N. Harris, and M. Horstwood (2011), A short-duration pulse of ductile normal shear on the outer South Tibetan detachment in Bhutan: Alternating channel flow and critical taper mechanics of the eastern Himalaya, *Tectonics*, **30**, TC2005, doi:10.1029/2010TC002784.
- Cooper, F. J., K. V. Hodges, and B. A. Adams (2013), Metamorphic constraints on the character and displacement of the South Tibetan fault system, central Bhutanese Himalaya, *Lithosphere*, **5**, 67–81, doi:10.1130/L221.1.
- Corrie, S. L., and M. J. Kohn (2011), Metamorphic history of the central Himalaya, Annapurna region, Nepal, and implications for tectonic models, *Geol. Soc. Am. Bull.*, **123**, 1863–1879, doi:10.1130/B30376.1.
- Corrie, S. L., M. J. Kohn, N. McQuarrie, and S. P. Long (2012), Flattening the Bhutan Himalaya, *Earth Planet. Sci. Lett.*, **349–350**, 67–74, doi:10.1016/j.epsl.2012.07.001.
- Dahlstrom, C. D. A. (1969), Balanced cross-sections, *Can. J. Earth Sci.*, **6**, 743–757.
- Daniel, C. G., L. S. Hollister, R. R. Parrish, and D. Grujic (2003), Exhumation of the Main Central Thrust from lower crustal depths, eastern Bhutan Himalaya, *J. Metamorph. Geol.*, **21**, 317–334, doi:10.1046/j.1525-1314.2003.00445.x.
- Dasgupta, S. (1995a), Shumar Formation, in *The Bhutan Himalaya: A Geological Account*, vol. 39, edited by O. N. Bhargava, pp. 64–78, Spec. Publ. Ser. Geol. Soc., India.
- Dasgupta, S. (1995b), Jaishidanda Formation, in *The Bhutan Himalaya: A Geological Account*, vol. 39, edited by O. N. Bhargava, pp. 79–88, Spec. Publ. Ser. Geol. Soc., India.
- Davidson, C., D. E. Grujic, L. S. Hollister, and S. M. Schmid (1997), Metamorphic reactions related to decompression and synkinematic intrusion of leucogranite, High Himalayan crystallines, Bhutan, *J. Metamorph. Geol.*, **15**, 593–612, doi:10.1111/j.1525-1314.1997.00044.x.
- Davis, D., J. Suppe, and F. A. Dahlen (1983), Mechanics of fold-and-thrust belts and accretionary wedges, *J. Geophys. Res.*, **88**, 1153–1172, doi:10.1029/JB088iB02p01153.
- DeCelles, P. G., D. M. Robinson, and G. Zandt (2002), Implications of shortening in the Himalayan fold-thrust belt for uplift of the Tibetan Plateau, *Tectonics*, **21**(6), 1062, doi:10.1029/2001TC001322.
- Drury, M. R., and J. L. Urai (1990), Deformation-related recrystallization processes, *Tectonophysics*, **172**, 235–253.
- Drury, M. R., F. J. Humphreys, and S. H. White (1985), Large strain deformation studies using polycrystalline magnesium as rock analogue, Part II: Dynamic recrystallization mechanisms at high temperatures, *Phys. Earth Planet. Inter.*, **40**, 208–222.
- Dunlap, W. J., G. Hirth, and C. Teyssier (1997), Thermomechanical evolution of a ductile Duplex, *Tectonics*, **16**, 983–1000, doi:10.1029/97TC00614.
- Dunnet, D. (1969), A technique for finite strain analysis using elliptical particles, *Tectonophysics*, **7**, 117–136.
- Dunnet, D., and A. W. B. Siddans (1971), Non-random sedimentary fabrics and their modification by strain, *Tectonophysics*, **12**, 307–325.
- Eppelbaum, L., I. Kutasov, and A. Pilchin (2014), *Applied Geothermics, Lecture Notes in Earth System Sciences*, 750 p, Springer, New York, doi:10.1007/978-3-642-34023-9\_2.
- Faleiros, F. M., R. Moraes, M. Pavan, and G. A. C. Campanha (2016), A new empirical calibration of the quartz c-axis fabric opening-angle deformation thermometer, *Tectonophysics*, **671**, 173–182, doi:10.1016/j.tecto.2016.01.014.
- Fitzgerald, J. D., and H. Stunitz (1993), Deformation of granitoids at low metamorphic Grade. I. Reactions and grain size reduction, *Tectonophysics*, **221**, 269–297.
- Flinn, D. (1962), On folding during three-dimensional progressive deformation, *Quart. J. Geol. Soc. Lond.*, **118**, 385–433.
- Fossen, H., and B. Tikoff (1993), The deformation matrix for simultaneous simple shearing, pure shearing and volume change, and its application to transpression–transtension tectonics, *J. Struct. Geol.*, **15**, 413–422.
- Gansser, A. (1964), *Geology of the Himalayas*, pp. 289, Wiley-Interscience, New York.
- Gansser, A. (1983), *Geology of the Bhutan Himalaya*, pp. 181, Birkhäuser, Basel, Switzerland.
- Gehrels, G. E., P. G. DeCelles, A. Martin, T. P. Ojha, and G. Pinhasi (2003), Initiation of the Himalayan Orogen as an early Paleozoic thin-skinned thrust belt, *GSA Today*, **13**, 4–9.
- Godin, L., D. Grujic, R. D. Law, and M. P. Searle (2006), Channel flow, ductile extrusion and exhumation in continental collision zones: An introduction, in *Channel Flow, Extrusion, and Exhumation in Continental Collision Zones*, edited by R. D. Law, M. P. Searle, and L. Godin, *Geol. Soc. London, Spec. Publ.*, **268**, 1–23.
- Grasemann, B., H. Fritz, and J. C. Vannay (1999), Quantitative kinematic flow analysis from the Main Central Thrust Zone (NW Himalaya, India): Implications for a decelerating strain path and the extrusion of orogenic wedges, *J. Struct. Geol.*, **21**, 837–853.



- Grujic, D., M. Casey, C. Davidson, L. Hollister, R. Kundig, T. L. Pavlis, and S. Schmid (1996), Ductile extrusion of the Higher Himalayan Crystalline in Bhutan: Evidence from quartz microfabrics, *Tectonophysics*, **260**, 21–43.
- Grujic, D., L. S. Hollister, and R. R. Parrish (2002), Himalayan metamorphic sequence as an orogenic channel: Insight from Bhutan, *Earth Planet. Sci. Lett.*, **198**, 177–191, doi:10.1016/S0012-821X(02)00482-X.
- Guillope, M., and J. P. Poirier (1979), Dynamic recrystallization during creep of single-crystalline halite: An experimental study, *J. Geophys. Res.*, **84**, 5557–5567, doi:10.1029/JB084iB10p05557.
- Harrison, T. M., F. J. Ryerson, P. LeFort, A. Yin, O. Lovera, and E. J. Catlos (1997), A late Miocene-Pliocene origin for the central Himalayan inverted metamorphism, *Earth Planet. Sci. Lett.*, **146**, E1–E7.
- Harrison, T. M., M. Grove, O. M. Lovera, and E. J. Catlos (1998), A model for the origin of Himalayan anatexis and inverted metamorphism, *J. Geophys. Res.*, **103**, 27,017–27,032, doi:10.1029/98JB02468.
- Henry, P., X. LePichon, and B. Goffe (1997), Kinematic, thermal and petrological model of the Himalayas: Constraints related to metamorphism within the underthrust Indian crust and topographic elevation, *Tectonophysics*, **273**, 31–56.
- Hodges, K. V. (2000), Tectonics of the Himalaya and southern Tibet from two perspectives, *Geol. Soc. Am. Bull.*, **112**, 324–350, doi:10.1130/0016-7606(2000)112<324:TOTHAS>2.0.CO;2.
- Holdaway, M. J. (2000), Application of new experimental and garnet Margules data to the garnet-biotite geothermometer, *Am. Mineral.*, **85**, 881–892.
- Jamieson, R. A., C. Beaumont, S. Medvedev, and M. H. Nguyen (2004), Crustal channel flows: 2. Numerical models with implications for metamorphism in the Himalayan-Tibetan orogen, *J. Geophys. Res.*, **109**, B06407, doi:10.1029/2003JB002811.
- Jessup, M. J., R. D. Law, M. P. Searle, and M. S. Hubbard (2006), Structural evolution and vorticity of flow during extrusion and exhumation of the Greater Himalayan Slab, Mount Everest Massif, Tibet/Nepal: Implications for orogen-scale flow partitioning, in *Channel Flow, Extrusion, and Exhumation in Continental Collision Zones*, edited by R. D. Law, M. P. Searle, and L. Godin, *Geol. Soc. London, Spec. Publ.*, **268**, 379–414.
- Johnson, S. E., H. J. Lenferink, N. A. Price, J. H. Marsh, P. O. Koons, D. P. West Jr., and R. Beane (2009), Clast-based kinematic vorticity gauges: The effects of slip at matrix/clast interfaces, *J. Struct. Geol.*, **31**, 1322–1339, doi:10.1016/j.jsg.2009.07.008.
- Kohn, M. J. (2008), P-T-t data from central Nepal support critical taper and repudiate large-scale channel flow of the Greater Himalayan Sequence, *Geol. Soc. Am. Bull.*, **120**, 259–273.
- Kohn, M. J. (2014), Himalayan metamorphism and its tectonic implications, *Annu. Rev. Earth Planet. Sci.*, **42**, 381–419.
- Kohn, M. J., M. S. Wieland, C. D. Parkinson, and B. N. Upreti (2004), Miocene faulting at plate tectonic velocity in the Himalaya of central Nepal, *Earth Planet. Sci. Lett.*, **228**, 299–310.
- Kruhl, J. H. (1996), Prism- and basal-plane parallel subgrain boundaries in quartz: A microstructural geothermobarometer, *J. Metamorph. Geol.*, **14**, 581–589.
- Kruhl, J. H. (1998), Prism- and basal-plane parallel subgrain boundaries in quartz: A microstructural geothermobarometer: Reply, *J. Metamorph. Geol.*, **16**, 142–146.
- Langille, J. M., J. Lee, B. R. Hacker, and G. Seward (2010), Middle crustal ductile deformation patterns in southern Tibet: Insights from vorticity studies in Mabja Dome, *J. Struct. Geol.*, **32**, 70–85, doi:10.1016/j.jsg.2009.08.009.
- Larson, K. P., and J. M. Cottle (2014), Midcrustal discontinuities and the assembly of the Himalayan midcrust, *Tectonics*, **33**, 718–740, doi:10.1002/2013TC003452.
- Larson, K. P., T. K. Ambrose, A. A. G. Webb, J. M. Cottle, and S. Shrestha (2015), Reconciling Himalayan midcrustal discontinuities: The Main Central thrust system, *Earth Planet. Sci. Lett.*, **429**, 139–146, doi:10.1016/j.epsl.2015.07.070.
- Law, R. D. (2010), Moine thrust zone mylonites at the Stack of Glencoul: II—Results of vorticity analyses and their tectonic significance, in *Continental Tectonics and Mountain Building—The Legacy of Peach and Horne*, edited by R. D. Law, et al., *Geol. Soc. London, Spec. Publ.*, **335**, 579–602, doi:10.1144/SP335.24.
- Law, R. D. (2014), Deformation thermometry based on quartz c-axis fabrics and recrystallization microstructures: A review, *J. Struct. Geol.*, **66**, 129–161, doi:10.1016/j.jsg.2014.05.023.
- Law, R. D., M. P. Searle, and R. L. Simpson (2004), Strain, deformation temperatures and vorticity of flow at the top of the Greater Himalayan Slab, Everest Massif, Tibet, *J. Geol. Soc. Lond.*, **161**, 305–320.
- Law, R. D., M. J. Jessup, M. P. Searle, M. K. Francis, D. J. Waters, and J. M. Cottle (2011), Telescoping of isotherms beneath the South Tibetan Detachment System, Mount Everest Massif, *J. Struct. Geol.*, **33**, 1569–1594, doi:10.1016/j.jsg.2011.09.004.
- Law, R. D., D. W. Stahr, M. K. Francis, K. T. Ashley, B. Grasemann, and T. Ahmad (2013), Deformation temperatures and flow vorticities near the base of the Greater Himalayan Series, Sutlej Valley and Shimla Klippe, NW India, *J. Struct. Geol.*, **54**, 21–53, doi:10.1016/j.jsg.2013.05.009.
- LeFort, P. (1975), Himalayas: The collided range. Present knowledge of the continental arc, *Am. J. Sci.*, **275-A**, 1–44.
- Lisle, R. J. (1977), Estimation of the tectonic strain ratio from the mean shape of deformed elliptical markers, *Geol. Minj.*, **56**, 140–144.
- Lisle, R. J. (1979), Strain analysis using deformed pebbles: The influence of initial pebble shape, *Tectonophysics*, **60**, 263–277.
- Lister, G. S. (1977), Crossed-girdle c-axis fabrics in quartzite plastically deformed by plane strain and progressive simple shear, *Tectonophysics*, **39**, 51–54.
- Lister, G. S., and U. F. Dornsiepen (1982), Fabric transitions in the Saxony granulite terrain, *J. Struct. Geol.*, **4**, 81–92.
- Lister, G. S., and B. E. Hobbs (1980), The simulation of fabric development during plastic deformation and its application to quartzite: The influence of deformation history, *J. Struct. Geol.*, **2**, 355–370.
- Lister, G. S., and P. F. Williams (1979), Fabric development in shear zones: Theoretical controls and observed phenomena, *J. Struct. Geol.*, **1**, 283–297.
- Long, S., and N. McQuarrie (2010), Placing limits on channel flow: Insights from the Bhutan Himalaya, *Earth Planet. Sci. Lett.*, **290**, 375–390, doi:10.1016/j.epsl.2009.12.033.
- Long, S. P., and E. Soignard (2016), Shallow-crustal metamorphism during Late Cretaceous anatexis in the Sevier hinterland plateau: Peak temperature conditions from the Grant Range, eastern Nevada, U.S.A., *Lithosphere*, **8**, 150–164, doi:10.1130/L501.1.
- Long, S. P., N. McQuarrie, T. Tobgay, D. Grujic, and L. Hollister (2011a), Geologic map of Bhutan, *J. Maps*, **v2011**, 184–192, doi:10.4113/jom.2011.1159.
- Long, S., N. McQuarrie, T. Tobgay, C. Rose, G. Gehrels, and D. Grujic (2011b), Tectonostratigraphy of the Lesser Himalaya of Bhutan: Implications for the along-strike stratigraphic continuity of the northern Indian margin, *Geol. Soc. Am. Bull.*, **123**, 1406–1426, doi:10.1130/B30202.1.
- Long, S., N. McQuarrie, T. Tobgay, and D. Grujic (2011c), Geometry and crustal shortening of the Himalayan fold-thrust belt, eastern and central Bhutan, *Geol. Soc. Am. Bull.*, **123**, 1427–1447, doi:10.1130/B30203.1.
- Long, S., N. McQuarrie, T. Tobgay, and J. Hawthorne (2011d), Quantifying internal strain and deformation temperature in the eastern Himalaya, Bhutan: Implications for the evolution of strain in thrust sheets, *J. Struct. Geol.*, **22**, 579–608, doi:10.1016/j.jsg.2010.12.011.

- Long, S. P., N. McQuarrie, T. Tobgay, I. Coutand, F. J. Cooper, P. W. Reiners, J. Wartho, and K. V. Hodges (2012), Variable shortening rates in the eastern Himalayan thrust belt, Bhutan: Insights from multiple thermochronologic and geochronologic datasets tied to kinematic reconstructions, *Tectonics*, *31*, TC5004, doi:10.1029/2012TC003155.
- Ludwig, K. R. (2008), *Users Manual for Isoplot v.4.15/Ex: A Geochronological Toolkit for Microsoft Excel*, pp. 76, Berkeley Geochronology Center Spec. Publ., Berkeley, CA.
- Mainprice, D. H., J. L. Bouchez, P. Blumenfeld, and J. M. Tubia (1986), Dominant c slip in naturally-deformed quartz: Implications for dramatic plastic softening at high temperature, *Geology*, *14*, 819–822.
- Mattauer, M. (1986), Intracontinental subduction, crust-mantle décollement and crustal-stacking wedge in the Himalayas and other collision belts, in *Collision Tectonics*, edited by M. P. Coward and A. C. Ries, *Geol. Soc. London, Spec. Publ.*, *19*, 37–50.
- McQuarrie, N., D. Robinson, S. Long, T. Tobgay, D. Grujic, G. Gehrels, and M. Ducea (2008), Preliminary stratigraphic and structural architecture of Bhutan: Implications for the along-strike architecture of the Himalayan system, *Earth Planet. Sci. Lett.*, *272*, 105–117, doi:10.1016/j.epsl.2008.04.030.
- McQuarrie, N., S. P. Long, T. Tobgay, J. N. Nesbit, G. Gehrels, and M. Ducea (2013), Documenting basin scale, geometry and provenance through detrital geochemical data: Lessons from the Neoproterozoic to Ordovician Lesser, Greater, and Tethyan Himalayan strata of Bhutan, *Gondwana Res.*, *23*, 1491–1510, doi:10.1016/j.gr.2012.09.002.
- McQuarrie, N., T. Tobgay, S. P. Long, P. W. Reiners, and M. A. Cosca (2014), Variable exhumation rates and variable displacement rates: Documenting a recent slowing of Himalayan shortening in western Bhutan, *Earth Planet. Sci. Lett.*, *386*, 161–174, doi:10.1016/j.epsl.2013.10.045.
- Means, W. D. (1989), Stretching faults, *Geology*, *17*, 893–896.
- Means, W. D. (1994), Rotational quantities in homogeneous flow and the development of small-scale structures, *J. Struct. Geol.*, *17*, 893–896.
- Means, W. D., B. E. Hobbs, G. S. Lister, and P. F. Williams (1980), Vorticity and noncoaxiality in progressive deformation, *J. Struct. Geol.*, *2*, 371–378.
- Mitra, G. (1994), Strain variation in thrust sheets across the Sevier fold-and-thrust belt (Idaho-Utah-Wyoming): Implications for section restoration and wedge taper evolution, *J. Struct. Geol.*, *16*, 585–602.
- Morgan, S., and R. D. Law (2004), Unusual transition in quartzite dislocation creep regimes and crystal slip systems in the aureole of the Eureka Valley-Joshua Flat-Beer Creek pluton, California: A case for anhydrous conditions created by decarbonation reactions, *Tectonophysics*, *384*, 209–231, doi:10.1016/j.tecto.2004.03.016.
- Mottram, C. M., C. J. Warren, D. Regis, N. M. W. Roberts, N. B. W. Harris, T. W. Argles, and R. R. Parrish (2014), Developing an inverted Barrovian sequence: insights from monazite petrochronology, *Earth Planet. Sci. Lett.*, *403*, 418–431, doi:10.1016/j.epsl.2014.07.006.
- Passchier, C. W. (1987), Stable positions of rigid objects in non-coaxial flow—A study in vorticity analysis, *J. Struct. Geol.*, *124*, 211–222.
- Passchier, C. W., and R. A. J. Trouw (2005), *Micro-tectonics*, 2nd ed., pp. 366, Springer, New York.
- Pecher, A. (1989), The metamorphism in the central Himalaya, *J. Metamorph. Geol.*, *7*, 31–41.
- Poirier, J. P., and A. Nicolas (1975), Deformation-induced recrystallization by progressive misorientation of subgrain-boundaries, with special reference to mantle peridotites, *J. Geol.*, *83*, 707–720.
- Powell, C. M., and P. J. Conaghan (1973), Plate tectonics and the Himalayas, *Earth Planet. Sci. Lett.*, *20*, 1–12.
- Rahl, J. M., K. M. Anderson, M. T. Brandon, and C. Fassoulas (2005), Raman spectroscopic carbonaceous material thermometry of low-grade metamorphic rocks: Calibration and application to tectonic exhumation in Crete, Greece, *Earth Planet. Sci. Lett.*, *240*, 339–354, doi:10.1016/j.epsl.2005.09.055.
- Ramsay, J. G. (1967), *Folding and Fracturing of Rocks*, pp. 560, McGraw-Hill, New York.
- Ramsay, J. G. (1969), The measurement of strain and displacement in orogenic belts, in *Time and Place in Orogeny, Special Publication*, vol. 3, edited by P. E. Kent, G. E. Satterthwaite, and A. M. Spencer, pp. 43–79, Geological Society, London.
- Ramsay, J. G., and M. I. Huber (1983), *Techniques of Modern Structural Geology*, vol. 1: Strain Analysis, pp. 307, Academic Press, London.
- Richards, A., R. Parrish, N. Harris, T. Argles, and L. Zhang (2006), Correlation of lithotectonic units across the eastern Himalaya, Bhutan, *Geology*, *34*, 341–344.
- Robinson, D. M., P. G. DeCelles, C. N. Garzione, O. N. Pearson, T. M. Harrison, and E. J. Catlos (2003), Kinematic model for the Main Central thrust in Nepal, *Geology*, *31*, 359–362, doi:10.1130/0091-7613(2003)031<0359:KMFTMC>2.0.CO;2.
- Robinson, D. M., P. G. DeCelles, and P. Copeland (2006), Tectonic evolution of the Himalayan thrust belt in western Nepal: Implications for channel flow models, *Geol. Soc. Am. Bull.*, *118*, 865–885.
- Royden, L. H. (1993), The steady state thermal structure of eroding orogenic belts and accretionary prisms, *J. Geophys. Res.*, *98*, 4487–507, doi:10.1029/92JB01954.
- Sanderson, D. J. (1982), Models of strain variation in nappes and thrust sheets: A review, *Tectonophysics*, *88*, 201–233.
- Schelling, D., and K. Arita (1991), Thrust tectonics, crustal shortening, and the structure of the far-eastern Nepal Himalaya, *Tectonics*, *10*, 851–862, doi:10.1029/91TC01011.
- Schmid, S. M., and M. Casey (1986), Complete fabric analysis of some commonly observed quartz c-axis patterns, in *Mineral and Rock Deformation: Laboratory Studies, Geophys. Monogr. Ser.*, vol. 36, edited by B. E. Hobbs and H. C. Heard, pp. 263–286, AGU, Washington, D. C.
- Schneider, C. A., W. S. Rasband, and K. W. Eliceiri (2012), NIH Image to ImageJ: 25 years of image analysis, *Nat. Methods*, *9*, 671–675.
- Searle, M. P., R. D. Law, L. Godin, K. P. Larson, M. J. Streule, J. M. Cottle, and M. J. Jessup (2008), Defining the Himalayan Main Central thrust in Nepal, *J. Geol. Soc. Lond.*, *165*, 523–534, doi:10.1144/0016-76492007-081.
- Stipp, M., H. Stunitz, R. Heilbronner, and S. M. Schmid (2002), The eastern Tonale fault zone: A 'natural laboratory' for crystal plastic deformation over a temperature range from 250° to 700°C, *J. Struct. Geol.*, *24*, 1861–1884.
- Suppe, J. (1983), Geometry and kinematics of fault-bend folding, *Am. J. Sci.*, *283*, 684–721.
- Tangri, S. K. (1995), Baxa Group, in *The Bhutan Himalaya: A Geological Account*, edited by O. N. Bhargava, *Geol. Soc. India, Spec. Publ.*, *39*, 38–58.
- Tikoff, B., and H. Fossen (1993), Simultaneous pure and simple shear: The unifying deformation matrix, *Tectonophysics*, *217*, 267–283.
- Tikoff, B., and H. Fossen (1995), The limitations of three-dimensional kinematic vorticity analysis, *J. Struct. Geol.*, *12*, 1771–1784.
- Tobgay, T., N. McQuarrie, S. Long, M. J. Kohn, and S. Corrie (2012), The age and rate of displacement along the Main Central Thrust in the western Bhutan Himalaya, *Earth Planet. Sci. Lett.*, *319–320*, 146–158, doi:10.1016/j.epsl.2011.12.005.
- Tracy, R. J., P. Robinson, and A. B. Thompson (1976), Garnet composition and zoning in the determination of temperature and pressure of metamorphism, central Massachusetts, *Am. Mineral.*, *61*, 762–775.
- Turcotte, D. L., and G. Schubert (2002), *Geodynamics*, 2nd ed., pp. 456, Cambridge Univ. Press, New York.
- Urai, J. L., W. D. Means, and G. S. Lister (1986), Dynamic recrystallization of minerals, in *Mineral and Rock Deformation: Laboratory Studies*, edited by B. E. Hobbs and H. C. Heard, *AGU Monogr.*, vol. 36, pp. 161–199, Washington, D. C., doi:10.1029/GM036p0161.
- van Daalen, M., R. Meilbronner, and K. Kunze (1999), Orientation analysis of localized shear deformation in quartz fibres at the brittle-ductile transition, *Tectonophysics*, *303*, 83–107.

- Vannay, J.-C., and B. Grasemann (2001), Himalayan inverted metamorphism and syn-convergence extension as a consequence of a general shear extrusion, *Geol. Mag.*, **138**, 253–276, doi:10.1017/S0016756801005313.
- Wallis, S. R. (1992), Vorticity analysis in a metachert from the Sanbagawa Belt, SW Japan, *J. Struct. Geol.*, **14**, 271–280.
- Wallis, S. R. (1995), Vorticity analysis and recognition of ductile extension in the Sanbagawa belt, SW Japan, *J. Struct. Geol.*, **17**, 1077–1093.
- Wallis, S. R., J. P. Platt, and S. D. Knott (1993), Recognition of syn-convergence extension in accretionary wedges with examples from the Calabrian Arc and the Eastern Alps, *Am. J. Sci.*, **293**, 463–495.
- Webb, A. A. G. (2013), Preliminary balanced palinspastic reconstruction of Cenozoic deformation across the Himachal Himalaya (northwestern India), *Geosphere*, **9**, 572–587, doi:10.1130/GES00787.1.
- Webb, A. A., A. Yin, M. T. Harrison, J. Celerier, and P. W. Burgess (2007), The leading edge of the Greater Himalayan Crystalline complex revealed in the NW Indian Himalaya: Implications for the evolution of the Himalayan orogen, *Geology*, **35**, 955–958, doi:10.1130/G23931A.1.
- White, S. (1977), Geological significance of recovery and recrystallization processes in quartz, *Tectonophysics*, **39**, 143–170.
- Whitney, D. L., and B. W. Evans (2010), Abbreviations for names of rock-forming minerals, *Am. Mineral.*, **95**, 185–187.
- Williams, P. F., D. Jiang, and S. Lin (2006), Interpretation of deformation fabrics of infrastructure zone rocks in the context of channel flow and other tectonic models, in *Channel Flow, Ductile Extrusion and Exhumation in Continental Collision Zones, Spec. Publ.*, vol. 268, edited by R. D. Law, M. P. Searle, and L. Godin, pp. 221–236, Geol. Soc. London.
- Yakymchuk, C., and L. Godin (2012), Coupled role of deformation and metamorphism in the construction of inverted metamorphic sequences: An example from far-northwest Nepal, *J. Metamorph. Geol.*, **30**, 513–535, doi:10.1111/j.1525-1314.2012.00979.x.
- Yardley, B. W. D. (1977), An empirical study of diffusion in garnet, *Am. Mineral.*, **62**, 230–242.
- Yin, A. (2006), Cenozoic tectonic evolution of the Himalayan orogen as constrained by along-strike variation of structural geometry, exhumation history, and foreland sedimentation, *Earth Sci. Rev.*, **76**, 1–131.
- Yin, A., and T. M. Harrison (2000), Geologic evolution of the Himalayan-Tibetan orogen, *Annu. Rev. Earth Planet. Sci.*, **28**, 211–280.
- Yonkee, A. (2005), Strain patterns within part of the Willard thrust sheet, Idaho-Wyoming-Utah thrust belt, *J. Struct. Geol.*, **27**, 1315–1343.
- Zeiger, K., S. M. Gordon, S. P. Long, A. R. C. Kylander-Clark, K. Agustsson, and M. Penfold (2015), Timing and conditions of metamorphism and melt crystallization in Greater Himalayan rocks, eastern and central Bhutan: Insight from U-Pb zircon and monazite geochronology and trace-element analyses, *Contrib. Mineral. Petrol.*, **169**, 47, doi:10.1007/s00410-015-1143-6.